AD-A239 488

UMENTATION PAGE

Form Approved
OMB No. 0704-0188

on is estimated to average 1 hour per response, including the time for reviewing instructions, searching existing data sources, gathering and maintaining the data needed, and completing and reviewing the collection of information. Send comments regarding this burden estimate or any other aspect of this collection of information, including suggestions for reducing this burden to Washington Headquarters Services, Directorate for Information Operations and Reports, 1215 Jefferson Davis Highway, Suite 1204, Arlington, VA 22202-4302, and to the Office of Management and Budget, Paperwork Reduction Project (0704-0188), Washington, DC 20503

1. AGENCY USE ONLY (Leave blank)	2. REPORT DATE	3. REPORT TYPE AND DATES COVERED
	June 1991	THESIS/DISSERTATION

4. TITLE AND SUBTITLE
A Search for Periodoicity in the X-ray Spectrum of Black Hole Candidate A0620-00

5. FUNDING NUMBERS

6. AUTHOR(S)
Kenneth Plaks, First Lieutenant

7. PERFORMING ORGANIZATION NAME(S) AND ADDRESS(ES)
AFIT Student Attending: Massachusetts Institute of Technology

8. PERFORMING ORGANIZATION REPORT NUMBER
AFIT/CI/CIA-91-063

9. SPONSORING/MONITORING AGENCY NAME(S) AND ADDRESS(ES)
AFIT/CI
Wright-Patterson AFB OH 45433-6583

DTIC
ELECTE
AUG 0 9 1991
S
C

10. SPONSORING/MONITORING AGENCY REPORT NUMBER

11. SUPPLEMENTARY NOTES

12a. DISTRIBUTION/AVAILABILITY STATEMENT
Approved for Public Release IAW 190-1
Distributed Unlimited
ERNEST A. HAYGOOD, 1st Lt, USAF
Executive Officer

12b. DISTRIBUTION CODE

13. ABSTRACT (Maximum 200 words)

91-07310

14. SUBJECT TERMS

15. NUMBER OF PAGES
73

16. PRICE CODE

17. SECURITY CLASSIFICATION OF REPORT	18. SECURITY CLASSIFICATION OF THIS PAGE	19. SECURITY CLASSIFICATION OF ABSTRACT	20. LIMITATION OF ABSTRACT

A SEARCH FOR PERIODICITY IN THE X-RAY SPECTRUM OF BLACK HOLE CANDIDATE A0620-00

by

Kenneth Plaks

B.S. Math/Physics, U.S. Air Force Academy

(1989)

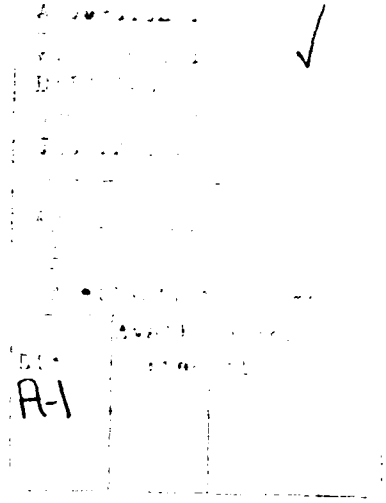

Submitted to the Department of
Physics in Partial Fulfillment of
the Requirements for the Degree of

MASTER OF SCIENCE

at the

MASSACHUSETTS INSTITUTE OF TECHNOLOGY

June 1991

© Kenneth Plaks, 1991, All rights reserved.
The author hereby grants to MIT permission to reproduce and to
distribute copies of this thesis document in whole or in part.

Signature of Author: .....
Department of Physics, June 1991

Certified by: George W. Clark
George W. Clark
Professor of Physics
Thesis Supervisor

Accepted by: .....
George F. Koster
Chairman, Departmental Committee on Graduate Studies

A Search for Periodicity in the X-Ray Spectrum of Black Hole Candidate A0620-00

by

Kenneth Plaks

Submitted to the Department of Physics on June 1,1991
in partial fulfillment of the requirements for the degree of
Master of Science in Physics

ABSTRACT

Using archival data from the MIT X-Ray Observatory on board the SAS-3 satellite, we have produced refined X-ray light curves of the X-ray nova A0620-00 during its initial outburst and subsequent decay. We use data from similar observations of the Crab Nebula to generate elevation dependent response functions for the SAS-3 detectors and to develop objective criteria for perfecting the A0620 data in the energy ranges 1.3 - 5 keV and 5 - 13 keV. We then analyzed the A0620 light curves and the hardness ratio for evidence of periodicity. In particular, we searched for evidence of the 7.75^{h} orbital period found in optical observations by McClintock and Remillard (1986). Using a Monte Carlo simulation, we showed that the 3σ upper limit on the amplitude of oscillation in the hardness ratio is 3.2%. We also searched for the 7.8^{d} period reported by Matilsky *et al.* (1976). We found three cycles of a 7.8^{d} oscillation in a 22 day section of the data with a ~ 40% amplitude. However in the remainder of the data, in excess of 200 days, we were able to place 3σ upper limits on the intensity amplitude of 2.2% before the section and 7.3% after. We therefore find no evidence to substantiate a persistent 7.8^{d} period. We conclude that the system exhibits little to no persistent X-ray periodicity at any frequency. We also conclude that high inclination angle models of the system where the accretion disk is fed via Roche lobe overflow are not appropriate.

Thesis Supervisor: Dr George W. Clark
Professor of Physics

Table of Contents:

Chapter 1 Introduction **1**
1.1 Black Holes 3
1.1.a Characteristics 4
1.1.b Useful Results from General Relativity 6
1.2 Steady State Accretion Disks 8
1.2.a Structure of the "Standard Disk" 8
1.2.b Spectrum of the "Standard" Disk 9
1.3 Non-Steady State Accretion Disks 12
1.4 Candidates 14
1.4.a Cygnus X-1 14
1.4.b LMC X-3 16
1.4.c A0620 17

Chapter 2 Data Reduction **20**
2.1 Fitting the Data 20
2.2 Systematic Corrections 22

Chapter 3 Application to A0620 ..... **31**

Chapter 4 Data Analysis **44**
4.1 Phase Dispersion Minimization 44
4.2 Results 48
4.2.1 Detrending the Data 48
4.2.2 Monte Carlo Simulation 61
4.2.3 MB's Data 65
4.3 Conclusions 67

References **69**

Acknowledgements **73**

Chapter 1: Introduction

On August 3, 1975 the British satellite Ariel V discovered the X-ray nova A0620 (Elvis *et al.* 1975). The MIT X-Ray Observatory on board NASA's SAS-3 satellite began observing it on August 8, 1975 and continued to observe it fairly regularly until February 13, 1976. The intensity of the nova rapidly rose to a peak value and for two months it was the brightest object in the X-ray sky. Using the X-ray position determined by Doxsey *et al.* (1976), Boley and Wolfson (1975) identified the optical counterpart and reported that the X-ray nova was accompanied by an outburst in the visible spectrum: the optical counterpart brightened from 18th to 12th magnitude. Following the initial discovery there were a flurry of observations across the electromagnetic spectrum. Craft (1975), Scott (1975), and Owen *et al.* (1976), identified a radio counterpart. The nova was observed in the radio by Little *et al.* (1976). It was observed in the infrared by Citterio *et al.* (1976) and Kleinmann *et al.* (1976). Carpenter *et al.* (1976), Lloyd *et al.* (1977), and Tsumeni *et al.* (1977) observed it in the optical. The Ariel V X-ray spectrum was observed by Ricketts (1975) and Kaluzienski *et al.* (1977) discussed the decay of the X-ray intensity as observed by Ariel V. The SAS-3 X-ray observations were analyzed by Matilsky *et al.* (1976), MB hereafter. Many spectroscopic studies were done including those by Coe *et al.* (1976), Wheelan *et al.* (1977), Oke *et al.* (1977), and Long *et al.* (1978).

After 15 months the system, a low mass binary with a compact component, returned to its pre-outburst brightness and has remained quiescent ever since. Using the Harvard plates, Eachus *et al.* (1976) found an outburst of the optical counterpart in 1917, and it seems likely that it too was accompanied by an X-ray nova. Photometric and spectroscopic studies by

McClintock and Remillard (1986), MR hereafter, demonstrated the system has a high mass function and placed a lower limit on the mass of the compact component which exceeds the theoretical maximum mass of a neutron star. This study sparked interest in A0620-00 as a black hole binary system.

In this paper, we analyze the X-ray data obtained from the detectors on the SAS-3 X-Ray Observatory, the instrumentation for which was designed and built at the MIT Center for Space Research. We use these data to search for evidence of the 7.75^{h} orbital period in the X-ray phenomena and to reexamine the evidence for the 7.8^{d} period reported by MB. In Chapter 1, we present background information on black holes and accretion disk systems relevant to a study of A0620 as a black hole candidate. We also review the three major black hole candidates and recount various researcher's observational evidence in favor of the candidates being black holes. In Chapter 2, we discuss how we processed and refined the SAS-3 data and describe how we used data from Crab Nebula observations to assess and correct systematic defects in the processing. In Chapter 3, we apply the criteria and procedures of Chapter 2 to A0620 to generate refined light curves that allow accurate detrending and thereby a more sensitive search for periodicities. In Chapter 4, we discuss the theory behind the period searching techniques employed and apply these techniques to generate limits on the observed X-ray periodicities of A0620.

1.1 Black Holes

When a star exhausts its available nuclear fuel, thermal pressure cannot stop its contraction. However, electron degeneracy pressure can sustain an evolved star against gravitational collapse as long as its mass does not exceed the Chandrasekhar limit of 1.4 $M_{\odot}$. Stars supported solely by electron degeneracy pressure are known as white dwarfs. They typically have a mass of about one $M_{\odot}$ and a radius of about 5000 km.

If a white dwarf's mass exceeds the Chandrasekhar limit, the electron degeneracy pressure is insufficient to resist the gravitational attraction. The star collapses. Electrons and protons merge via inverse beta decay and become neutrons. Total collapse is prevented by neutron degeneracy pressure. Stars supported by neutron degeneracy pressure are called neutron stars. They are observed as radio pulsars and as the X-ray emitting components of binary X-ray sources.

The limits of stability of neutron stars are not completely understood. Rotation, and the equation of state (which is not precisely known) are essential determinants of the critical mass. However, within the framework of general relativity one can derive an upper limit based on considerations of causality, which restricts the equation of state so as to yield a speed of sound less than the speed of light. According to Shapiro and Teukolsky (1983) (ST hereafter), the mass limit is probably about 2.7 $M_{\odot}$ with an absolute causality limit of ~ 3 - 5 $M_{\odot}$.

1.1.a Characteristics

In theory four observables characterize a black hole: charge, angular momentum, radius, and mass.

Since celestial objects are embedded in conducting plasmas, they cannot sustain a condition of substantial electrical charge under any circumstances.

The angular momentum of a black hole affects the position of the event horizon and can in principle create certain interesting mechanical and optical effects. However, these effects are difficult if not impossible to observe at astronomical distances.

The radius of a black hole is its event horizon at which unique optical phenomena could, in principle, be detected by visual means. However the angular resolution required for the nearest possible black hole is hopelessly unattainable. It appears, therefore, that the only feasible method for detecting and characterizing a black hole at astronomical distances is through measurement of its mass and its identification as a collapsed star.

If the object happens to be in a binary system, then we can observe its effect on its visible companion. Using Kepler's third law, one can relate the companion's semimajor axis, period, and mass (obtainable through its spectral type) to the mass of the compact object. A convenient formula for relating the observed orbital parameters to the compact object's mass is the mass function

$$f(M_1, M_2, i) = \frac{(M_2 \sin i)^3}{(M_1 + M_2)^2} = \frac{P v_1^3}{2\pi G} \qquad (1.1.a.1)$$

where M_1 is the mass of the optical companion star, M_2 is the mass of the compact object, i is the inclination angle, and v_1 is the projection of the orbital velocity along the line of sight of the observer (see figure 1.1). The mass function depends only on the observables P, v_1, and i and is equal to the minimum possible value of M_2 which occurs when $M_1 = 0$ and sin i is a maximum (i = 90°). In chapter 1.4 I will show how others have applied the mass function mass determination method to estimate the masses of CYG X-1, LMC X-3, and A0620.

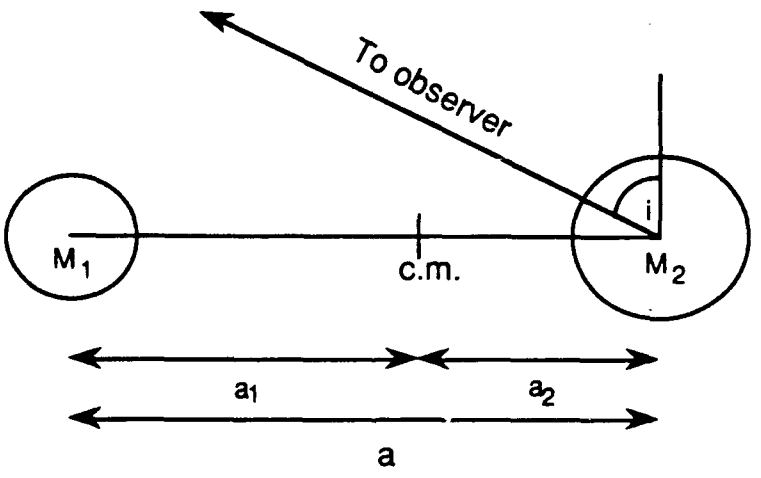

Figure 1.1: The parameters of the binary black hole system. M_1 is the star, M is the hole, and i is the inclination angle with respect to the observer.

1.1.b Useful Results from General Relativity

From the minimization of the general relativistic action, it can be shown (ST) that the specific energy, e, of a test particle in a circular orbit about a non-rotating black hole is given by

$$e = \frac{r - 2M}{\sqrt{r(r - 3M)}} \qquad (1.1.b.1)$$

where r is the radius of the orbit, M is the mass of the central body and the "geometrized" units G = c = 1 have been used. While circular orbits exist all the way down to r = 3M, they are only stable down to r = 6M. Within r = 6M a small perturbation will cause the particle to spiral rapidly into the central object. Substituting r = 6M into equation (1.1.b.1) one obtains the binding energy of the last stable orbit

$$E_{binding} = (m - E)/m = 1 - e = 5.72\% \qquad (1.1.b.2)$$

This represents the fraction of its rest mass energy that a particle originally at rest at infinity releases as it spirals down to the last stable circular orbit and before it plunges into the hole. The release of gravitational energy is evidently a very efficient means of energy production, a conclusion that motivates the idea that accretion by a black hole may explain the huge luminosities that some compact objects generate.

More complicated is the Kerr (rotating) black hole. We define the angular momentum per unit mass a = J/M. When a = 0 one returns to the

Schwarzschild (non-rotating) case. If a = M then the black hole is said to be maximally rotating. As in the Schwarzschild case, one can solve for the specific energy which can be shown to be

$$e = \frac{r^2 - 2Mr \pm a\sqrt{Mr}}{r\sqrt{r^2 - 3Mr \pm 2a\sqrt{Mr}}} \qquad (1.1.b.3)$$

where the upper sign is for a corotating (direct) orbit and the lower sign is for a counterrotating (retrograde) orbit. A quantity of particular interest is the binding energy of the last stable circular orbit for a maximally rotating black hole. When a = M, the radius of the marginally stable orbit is r_{ms} = M (direct), or 9M (retrograde). For a direct orbit at this radius and angular momentum, $e = (1/3)^{1/2}$ and the binding energy, which as before represents the fraction of rest energy released by a particle initially at rest at infinity, is

$$\varepsilon_{binding} = 1 - e = 42.3\%! \qquad (1.1.b.4)$$

One can see that the release of gravitational binding energy is a phenomenally efficient means of energy production. This is why black holes have been invoked to explain objects from Quasars to active galactic nuclei.

In section 1.2 I will present the results of the Keplerian approximation to an accretion disk about a black hole and show that the disk strongly radiates in the soft X-ray regime. We shall see that the accretion disk model motivates us to identify super luminous X-ray sources as black hole accretion disks.

1.2 Steady State Accretion Disks

Accretion disks account for the black hole's remarkable efficiency in the conversion of gravitational binding energy into X-ray luminous energy. As shown in section 1.1, while spherical accretion can give rise to conversion efficiencies on the order of 5% of the rest mass, a disk about a rotating black hole can have conversion efficiencies of up to 40% mc^2.

In general, matter flowing toward a black hole is expected to form an accretion disk in a binary system. The two primary mechanisms by which mass can be injected into the black hole's gravitational well are Roche lobe overflow and stellar wind capture. Both mechanisms inject mass into the black hole's gravitational well with an angular momentum per unit mass which is proportional to that of the binary system. Some of the injected mass is thrown off, and some is accreted. Since the accreted mass has angular momentum with respect to the black hole, the mass cannot enter the hole directly, but must form a disk orbiting in the plane of the system. Through viscous stresses the matter in the disk looses angular momentum and spirals inward until it looses sufficient angular momentum to bring it within the last stable orbit predicted by general relativity. Only then can it enter the hole.

The goal of this chapter is to review the theory of accretion disks about black holes and to show why one expects an accretion disk to radiate in the soft X-ray regime for it was through its X-ray radiation that A0620 was identified as a compact object.

1.2.a Structure of the "Standard Disk"

In can be shown (Shakura and Sunyaev (1973), and ST) that by employing conservation laws, an equation of state, a viscosity law, and a radiative transport law that one can derive the basic structures and spectra of an accretion disk. The structures and spectra of the disk, in turn, are functions of three parameters: the radius, r, the mass of the central object, M, and and the mass accretion rate, $\dot{M}$. For fixed values of these three parameters the disk can be conveniently divided into three regions.

1. An inner region where radiation pressure and scattering dominate.

2. A middle region where the dominant source of opacity is scattering, but gas pressure dominates radiation pressure. The transition between the inner and middle regions occurs at the radius r_{mi} where $P_g = P_{rad}$.

3. An outer region, at large r, where gas pressure dominates radiation pressure and the opacity is dominated by free-free absorption. The transition from the outer to the middle region occurs at a radius, r_{om}, where $\kappa_{ff} \sim \kappa_{es}$.

1.2.b Spectrum of the "Standard" Disk

The standard model predicts disk temperatures on of the order $T \approx 10^7$K. When attempting to interpret the spectrum of the disk, it is important to realize that the temperature calculated in the standard model is the temperature at midplane (z=0). The observable temperature however is the temperature at the effective emitting surface, where the photons which escape to infinity are generated. We expect the surface temperature, T_s to be less than the midplane temperature except when the disk is optically thin, in which case photons generated at the center escape. For optically thick disks in regions where absorption dominates scattering, the emission has a blackbody spectrum with characteristic temperature T_s, which is the temperature of the disk at an optical depth $\bar{\tau}_{ff} \sim 1$ below the surface where the average escaping photon is generated. Therefore the emission spectrum is that of a blackbody in the outer regions, $r > r_{om}$, where absorption dominates scattering. It can be shown that in these regions, $T_s \leq 10^5$K.

In the middle to inner regions, scattering dominates absorption and the blackbody approximation no longer holds. Following emission, the photons undergo many scatterings which can best be characterized as a random walk. This scattering generates a modified blackbody distribution. It can be shown that the effective blackbody temperature is approximately

$$T_{eff} \approx T_s \left(\frac{\kappa_{ff}}{\kappa_{es}}\right)^{1/8} \qquad (1.2.b)$$

where the Rosseland mean opacity is used to evaluate the parentheses. Since it is assumed that $\kappa_{ff} << \kappa_{es}$ it stands that $T_s >> T_{eff}$. Since T_s represents the

mean temperature of the region emitting the photons, one can see that the effect of scattering is to *raise* the mean energy of the emitted photons ($\sim kT_s$) above the blackbody value at thermodynamic equilibrium. It can be shown that in these regions T_s is on the order of 10^6 - 10^7K and therefore their emission is "harder."

In the innermost regions, Comptonization becomes important. In this process, photons are scattered by relativistic electrons. These regions are even hotter, reaching T $\leq 10^8$ K. Figure 1.2.b shows a typical power spectra.

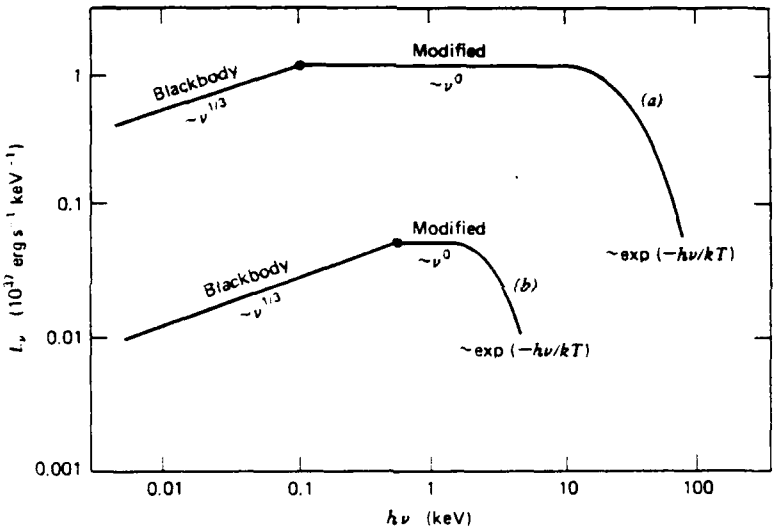

Sketch of the power spectra emitted by two model disks around black holes, as calculated by Shakura and Sunyaev (1973) without taking account of relativistic corrections or capture of radiation by the hole. In both models the hole was assumed to be nonrotating, so the inner edge of the disk was at $r_I = 6M$. Model (a) corresponds to $\alpha \sim 10^{-3}$, $M = M_\odot$, $\dot{M} = 10^{-8} M_\odot$ yr^{-1}, $L = L_{Edd} \approx 10^{38}$ erg s^{-1}; model (b) corresponds to $\alpha \sim 10^{-2}$ to 1 (spectrum insensitive to α), $M = M_\odot$, $\dot{M} = 10^{-6} M_\odot$ yr^{-1}, $L \approx 10^{36}$ erg s^{-1}. The portion of the spectrum marked "blackbody" is generated primarily by the outer, cold region of the disk where electron scattering is unimportant. The portion marked "modified" is generated by the middle and inner regions where electron scattering is the dominant source of opacity. The temperature of the exponential tail is the surface temperature of the innermost region. [From Novikov and Thorne (1973).]

Figure 1.2.b: Typical accretion disk spectrum (ST).

1.3 Non-Steady State Accretion Disks

The steady state results presented in chapter 1.2 are insufficient to explain the transient nature of X-ray sources such as A0620. Attempts to model these types of sources fall into two categories: disk instability models and mass transfer instability models.

Within the disk instability picture there are two schools of thought. Mineshige and Wheeler (1989), Mineshige, Tuchman and Wheeler (1990) and Huang and Wheeler (1989), HW hereafter, claim that it is possible to set up temperature and density waves in the disk as it accretes. They assume a constant low mass transfer rate, a two temperature viscosity parameter, and a temperature dependent opacity to account for atomic and molecular absorption. This leads to a double valued relationship between temperature and surface density and the model undergoes a subcritical pitchfork bifurcation into two stable surface densities, a lower value Σ_{cold} and a higher value Σ_{hot}. When the interior of the slowly accreting disk surpasses Σ_{hot}, a heating wave propagates outward and causes what HW call a "minor" outburst. If the heating wave propagates far enough out it can trigger an inward propagating cooling wave which causes the disk to accrete strongly in order to lower the surface density to Σ_{cold} in the inner regions. This corresponds to what HW call a "major" burst such as the 1975 burst of A0620. One can choose the free parameters and boundary conditions in this model to give good agreement with the A0620 outburst.

Other disk instability models (Canizzo *et al.* 1982; Lin and Taam 1984) are reminiscent of models for dwarf novae outbursts in which a low accretion rate causes the density of the disk to slowly build up until the disk

becomes optically thick. At this point the disk undergoes convection which rapidly transports matter onto the compact object creating a nova.

Mass transfer instability theories attribute the nova to the companion. Hameury *et al.* (1986) claim that hard X-rays from accretion can induce an instability in the photosphere of the companion. At the inner Lagrangian point, hard X-rays can penetrate just below the photosphere, heating it. This X-ray heating expands the atmosphere at L1 causing an envelope of extended stellar atmosphere to form. When the distance between the extended atmosphere and L1 reaches a critical value, matter rapidly streams across the L1 point and onto the accretion disk. This increases the hard X-ray flux from accretion which increases the X-ray heating of the companion which causes more matter to enter the envelope, etc. This positive feedback continues until the disk becomes optically thick, shielding the L1 point and quenching the instability. The nova then decays until the disk exhausts most of its mass. The authors point out that the key to testing this theory is observation of hard X-rays. Soft X-rays will be absorbed by the photosphere and merely expand the corona, not the atmosphere.

All of the above models predict recurrent novae and there are sufficient free parameters to match the tentative ~ 70 year period between bursts for A0620.

1.4 Candidates

There are three binary x-ray sources for which there is strong evidence of their being black holes. In each case the mass predicted by the mass function is large ($M_2 \sim 3M_\odot$), there is flux variability on short time scales implying compact size, and the X-ray luminosity is huge ($L \sim 10^{37}$ erg/s $\sim 10^4 L_\odot$). The three candidates are CYG X-1, LMC X-3, and A0620. In this section all data such as mass functions, luminosities, distances, periods, etc are taken from the concise summary given by McClintock (2333) unless otherwise stated.

1.4.a Cygnus X-1

Perhaps the best known of all black hole candidates, CYG X-1 was the first to be proposed to be a black hole in a binary system. The compact object has a mass function (equation 1.1.a.1) of $.25 \pm .01\ M_\odot$, which taken alone is not convincing evidence for it to be a black hole binary.

The optical companion is an O9.7 supergiant, HDE226868. If we assign a typical mass to HDE226868 of $33M_\odot$ then the mass of the compact object cannot be less than $7M_\odot$. However, it is possible that a companion in a close binary system may be severely undermassive for its spectral type (McClintock 2333; Paczynski 1973; van den Heuvel 1983) and thus the mass of the compact could be substantially less.

A second way of determining the mass comes from stellar structure calculations. While the supergiant may be undermassive, it can be shown (ST, Kippenhahn 1969) that the mass must be at least $8.5\ M_\odot$ to have the correct luminosity at a distance $d \sim 2$ kpc. The distance, d, can be found by measuring several stars within about a degree of HDE226868 and averaging the absorption and then using this absorption to adjust the reddening-distance

measurements. Two groups have done this and concluded that "HDE 226868 is not closer than 1 kpc, and that its minimum distance is about 2.5 kpc" (McClintock 2333; Bregman *et al.* 1973). Using 8.5 $M_\odot$ for the mass of the optical star, from the mass function we obtain a mass of $M_2 \geq 3.3\ M_\odot$.

According to Paczynski (1974), more conclusive evidence for CYG X-1 to be a black hole comes from the lack of X-ray eclipsing. In this event, limitations can be placed on the inclination of the orbital plane with respect to terrestrial observers and nothing has to be assumed about the mass of the supergiant. Following ST, if there is no eclipsing, it must be true that (see figure 1.4.a) $\cos i > R/a$

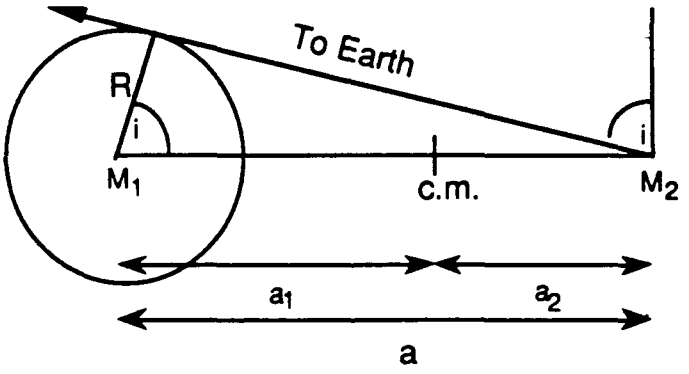

Figure 1.4.a No eclipse condition

It can be shown that the no eclipse condition translates into requiring that $M_2 \sin i \cos^2 i \geq fR^2/(a_1 \sin i)^2$. For a lower bound on M_2 one substitutes in $(\sin i \cos^2 i)_{max} = 2/3\sqrt{3}$.

One can relate R^2 to its luminosity and effective temperature to get an overall result of

$$M_2 \geq \frac{3\sqrt{3}\ f\ L_\odot}{8\pi\sigma T^4 (a_1 \sin i)^2} \left(\frac{d}{1\ kpc}\right)^2 10^{4+0.4(4.72-m_v-BC+A_v)} \quad (1.4.a.1)$$

where m_v is the apparent magnitude in the V, BC is to bolometric correction and A_v is the absorption in the V. Evaluating this expression with the parameters of CYG X-1, one finds that

$$M_2 \geq 3.4\ M_\odot \left(\frac{d}{2\ kpc}\right)^2 \quad (1.4.a.2)$$

If $d \geq 2$ kpc then this is very probably a black hole; if the distance is less, then we cannot say for sure. For example, if $d = 1.5$ kpc then $M_2 = 1.9\ M_\odot$.

If the supergiant is required not to overflow its Roche lobe then from ST $M_2 \geq 6.5\ M_\odot$ ($d = 2$ kpc). From all of these considerations one is forced to conclude that the mass of CYG X-1 probably exceeds $3\ M_\odot$ and therefore, since it cannot be a neutron star, it is probably a black hole.

1.4.b LMC X-3

LMC X-3 is a better candidate for two reasons. It has a mass function $f = 2.3 \pm 0.3\ M_\odot$ which exceeds the maximum neutron star mass in some models. Secondly, since it is in the Large Magellanic Cloud, its distance is known to be $d = 55$ kpc with small uncertainty.

Since LMC X-3 exhibits no x-ray eclipse one can use formula (1.4.a.1) with the appropriate parameters to give $M_2 > 6\ M_\odot$. If a typical mass for the

optical companion's spectral type is attributed to it, one finds $M_2 > 7\ M_\odot$ (McClintock 2333; Cowley *et al.* 1983).

1.4.c A0620

In chapter 1.2 it was shown that an accreting compact object could have a huge luminosity in the soft X-ray region of the spectrum. It is difficult to find another credible physical process which could produce this type of spectrum and luminosity. The luminosity of A0620 in soft X-rays was ~ 10^{38} erg s^{-1}. Therefore it is certainly a compact object.

The strongest evidence that A0620 is a black hole and not a neutron star is, first and foremost, its optical mass function which is $3.18 \pm 0.16\ M_\odot$ (MR). Thus, in the unphysical limit of a zero mass optical companion, this is the minimum mass of the compact object. This mass is much greater than the maximum mass of a neutron star in almost all current theories. From the observed mass function one can derive an absolute 3σ lower limit on the mass of the compact object of $M_2 = 2.7\ M_\odot$.

One can get a firm lower limit by assuming that the optical companion star is a zero age main sequence star. An average mass for a K dwarf is ~ 0.5 to 0.8 $M_\odot$. Paczynski(1973) and van den Heuvel(1983) have shown that binary accreting systems may have undermassive optical companions. Therefore a minimal mass of 0.25 $M_\odot$ is chosen for the companion. Since there is no X-ray eclipsing a credible maximum, $i = 85°$, is chosen. Choosing a velocity, v_1, of the K star which is 3σ less than the best fit value one obtains a 3σ lower limit of 3.20 $M_\odot$.

One can find a realistic mass by assuming a K5V star with a mass of $0.7M_\odot$. This is the preferred spectral type and mass for the K dwarf . In this

case the 3σ limit is $M_2 > 4.0\ M_\odot$. If one further requires the dwarf to fill its Roche lobe and the value suggested by the amplitude of ellipsoidal variations of $i < 50°$ is used for the inclination, one finds $M_2 > 7.3\ M_\odot$ (3σ).

Another method of placing a limit on the mass of the compact object has been suggested by Johnston *et al.* (1989). They observed the Doppler shifts of the H_α and H_β lines in the disk and fitted them to an accretion model and then averaged over several measurements to obtain a profile similar to 1.4.c.

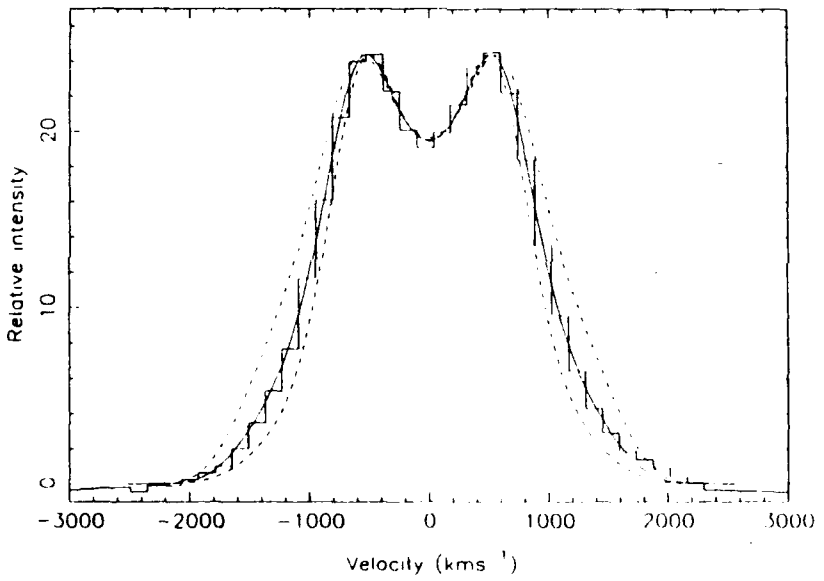

Figure 1.4.c Summed profile of all H_α spectra (Johnston *et al.*)

Using this profile, they were able to make an estimate of the velocity at the outer edge of the disk. Assuming the accretion disk is in the binary plane and that the velocity profile is given by circular Keplerian orbits, $v(r)=\sqrt{GMx/r}$, the outer edge represents the minimum velocity. If one requires that the

outer edge of the disk be within the Roche lobe of the black hole then, solving numerically, the absolute 3σ lower limit is $M_2 \geq 4\ M_\odot$ if $M_1=0.25\ M_\odot$. If the mass of the companion is $0.7\ M_\odot$, then the absolute 3σ lower limit is $M_2 \leq 9.3\ M_\odot$.

In summation, we see that there are several strong black hole candidates. A0620 is the most convincing of the three.

Chapter 2: Data Reduction

In this chapter, I discuss the various computer codes which were used to reduce the raw data from the SAS-3 satellite. I also explain how errors were assessed on the individual measurements. I examined data from observations of the Crab Nebula to obtain objective criteria for the selection and rejection of fitted data points and obtain elevation dependent response functions for the slat collimators. Finally, I discuss the probable systematic error induced into the data set.

2.1 Fitting the Data

The software packages used to reduce the data are *nbin*, *aspect*, *clean* and *fit* all of which were written by Richard Brezina. The program *nbin* decodes the data from the SAS-3 data archives and places it in tabular format. *Aspect* is used to determine satellite position, field of view for the detector of interest and, where applicable, the transmission function for the source at a given moment in time. *Clean* separates out source scans in the data stream output by *aspect* and attaches a portion of the data stream before and after the scan for background calculations. It also insures that there were occultations neither by the Earth nor the Moon and checks for the South Atlantic Anomaly, any of which is grounds to discard the scan. *Fit* then generates the relevant statistics. For a given orbit each routine is performed. I will only discuss *fit* in detail.

The *fit* program fits scanning-mode data to the triangular transmission function generated by *aspect* as shown in figure 2.1 (next page). It tries to correct for satellite timing errors by matching up the maxima of the least

squares fit of the *aspect* calculation and the actual scan. The fit is performed using the *curfit* routine given in Bevington (1969). The routine returns a fitted intensity, I_0, a fitted count rate for each measurement time, and the χ^2 for each fit with typical reduced $\chi^2 \approx 1.0$. We define the error in I_0 by

$$\sigma_{stat} = \frac{\sqrt{\sum counts + (scan\ duration) x (average\ background\ rate)}}{\int (transmission\ function) dt} \qquad (2.1.1)$$

where $\sum$counts is the total counts in the scan and transmission function is the percent transmission of the source during each time bin. Thus (2.1.1) represents the Poisson error associated with the source, but not errors in the transmission function determined by *aspect*. In chapter 2.2, I address this problem

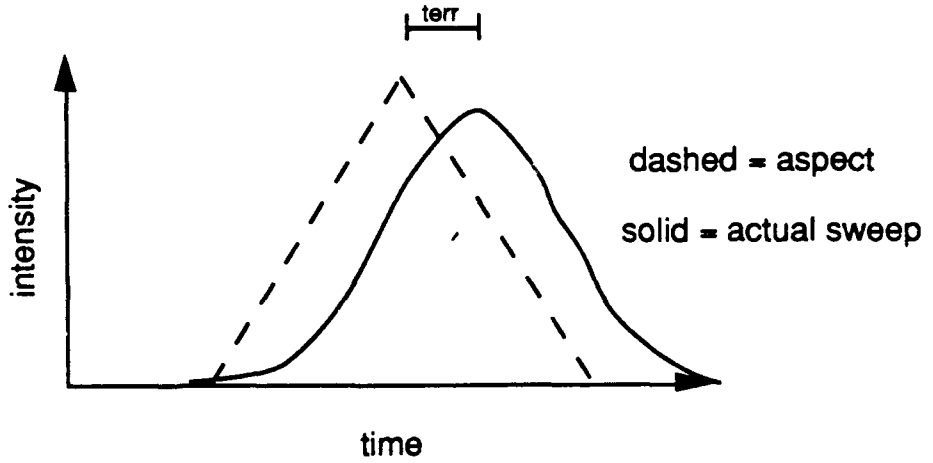

figure 2.1: Typical data scan. Fit adjusts the temporal position of the aspect curve by χ^2 minimization

2.2 Systematic Corrections

In an effort to assess the systematic errors in the intensities derived from A0620 data, we analyzed similar data on the Crab Nebula. Since the Crab is a steady source on all time scales longer than ~ 1 second, any systematic deviations of the computed intensity away from a constant value is a symptom of error which may also affect the accuracy of the computed A0620 intensities. Using the Crab as our standard "candle" we derived objective empirical criteria for selection and correction of the A0620 intensities. We also derived a response function for each channel which corrects for the systematic variation of intensity with elevation angle. In the following section, when we speak of data points we are refering to the fitted intensity generated by *fit* using the raw SAS-3 count data. Using the center slat A channel as an example, we describe how the tasks were accomplished in seven steps.

1. Purification

We discard any data points where A0620 and Crab are simultaneously in the channel's field of view. This can be done trivially by comparing crossing times and sweep durations. Figure 2.2a illustrates the raw Crab data and figure 2.2b shows the data after purification.

2. Remove Poor Fits and Excessive Timing Errors

We discard points for which the reduced χ^2 of the triangle fit to the scanning-mode data is greater than two. We do this since we are ultimately going to try to derive an elevation dependent response function based on the data and we only want to use our best data.

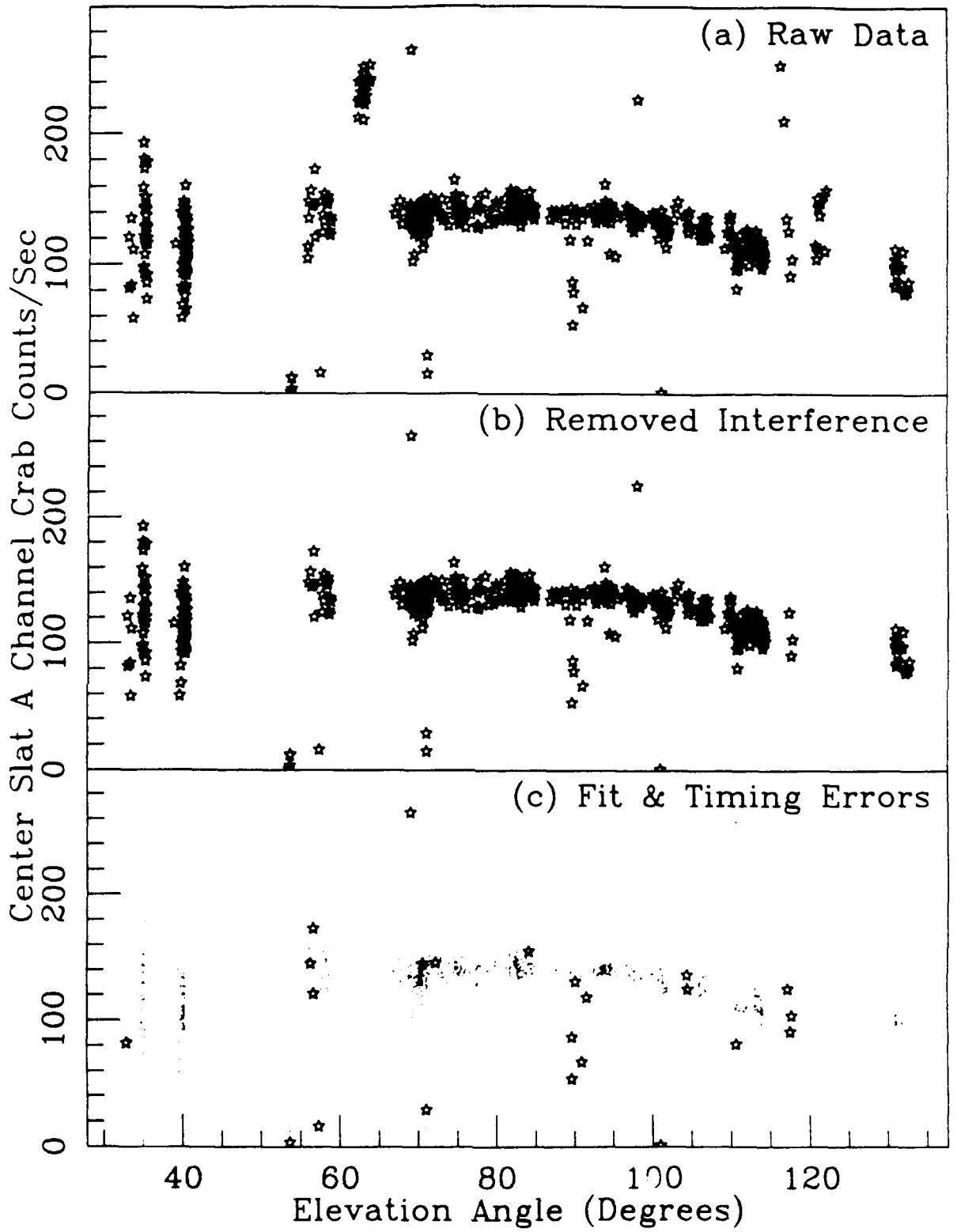

Figure 2.2: (a) The unprocessed intensity fits.
(b) The data after removing scans when A0620 was also in the field of view
(c) Points with $\chi^2 > 2$ and timing errors > ±8.64 seconds shown as stars.

We also remove points with excessive timing errors. By excessive we mean greater than ± 8.64 seconds = 10^{-4} day. The reason behind this discarding is that large timing errors represent data points with questionable spacecraft attitude information. In figure 2.2c, points removed by these screening criteria are shown as stars.

3. Removal of Other Less than Desirable Points

All of the reduction software is designed to be used on SAS counting rates obtained in the scanning mode. A typical scan over a source lasts for 15 - 45 seconds. Counts obtained in the pointing mode are not handled at all by these routines. Ultra-fast sweeps ($\Delta t < 8$ sec) are not handled well. Therefore we remove all points derived from scans with duration not in the range $8 \leq \Delta t \leq 50$ seconds.

Another source of error is high background count rates. For background determinations we use data from 100 seconds before and after each scan. If another smaller source enters the detector field of view during these background margins, it will perturb the apparent background rate. Since we subtract the background count rate from the source count rate, this can lead to inaccurate results. We therefore define the signal to noise ratio (SNR) to be I_0/b where b is the background count rate and I_0 is the fitted intensity. For the high count rate A and B channels we allow SNR ≥ 5. For the C channel, which has a lower count rate, we are forced to accept SNR ≥ 2. For the extremely low count rate D channel we accept any point with SNR ≥ 1.4.

Finally, we discard data for which $\sigma/I_0 > \frac{1}{2}$. Such a point is of little statistical significance since its error bars are so large. Figure 2.2d shows these other less than desirable points as stars.

4. Remove Points Outside the FWHM

As can be seen from figure 2.2d, points outside ±35° are unreliable. We therefore remove these points.

5. Window Elevation Angle Corrections

The beryllium windows on the slat detectors absorb soft X-rays. If a photon crosses the window at an angle, θ, the effective thickness of the window is increased by the factor $\sec\theta$ which causes increased absorption. To correct for this effect we calculate the window transmission at a particular angle, $t_x(\theta)$. We then relate this value to the transmission to the value at $\theta = 0$ by the percent transmission formula

$$t_x(\theta) = \frac{1}{t_x(0)} \int_{E_{min}}^{E_{max}} \exp[-T\mu_{Be}\sec\theta]\exp[-\sigma(E)N_H]E^{-\alpha}dE \quad (2.2.1)$$

where $\sigma(E)$ is the energy dependent interstellar photoelectric absorption cross section, N_H is the hydrogen column density, α is the spectral index, μ_{Be} is the mass absorption coefficient for beryllium, T is the thickness of the window, E_{min} and E_{max} are the channel boundaries of the detector in question and we have turned the transmission at an angle into a percentage of the transmission at $\theta = 0$ by dividing by $t_x(0)$, the window transmission function at 0°. From Woo(1991) the photon distribution in the energy

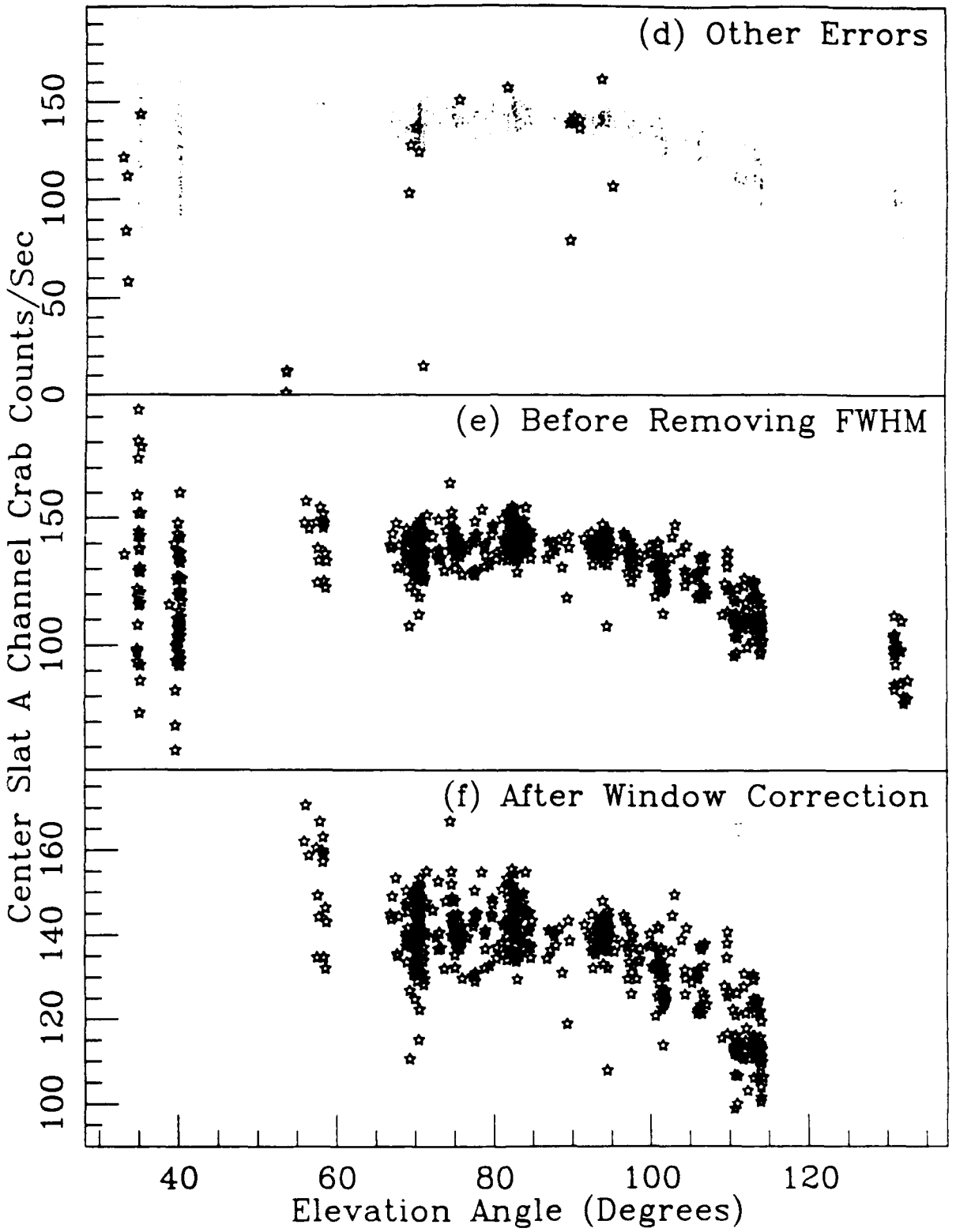

Figure 2.2: (d) Points with SNR < .5, $\sigma/I_0 > .5$ and not from scans depicted as stars.
(e) The data before removing points outside the FWHM.
(f) The data after window correction.

bands of interest can be fit by using $N_H = 3.45 \times 10^{21}$ particles/cm^2 and $\alpha = 2.1$. The data are then corrected as

$$I_0' = I_0/t_x(\theta)$$
$$\sigma' = \frac{\sigma}{I_0} I_0' = \sigma/t_x(\theta) \qquad (2.2.2)$$

where I_0 is the fitted intensity and σ is the Poisson error associated with it. In equation (2.2.2) we maintain the same percentage error bars i.e. if we knew I_0 to within, say, 10% before the correction, we still know it to within 10% after correction. We maintain relative error bars because we are correcting the data for systematic effects. Later in this chapter, I will discuss assessing additional systematic errors based on these systematic effects.

Figure 2.2e shows the data after the window correction. One can see that there is a systematic trend with respect to elevation. We now proceed to correct for this effect.

6. Generate the Systematic Correction Function.

We now generate the systematic correction function due to elevation angle, θ through an iterative process:

1. Fit the data to a 3rd order polynomial $y = a + b\theta + c\theta^2 + d\theta^3$.
2. Subtract the quadratic and cubic terms $c\theta^2 + d\theta^3$.
3. Set avg = the average of the new (nearly) linear data set.
4. Refer back to the original (pre-polynomial fit) data set and remove any points which are more than 3σ away from the average, avg, calculated in step 3.
5. Repeat from step 1 until no points are discarded in step 4.

Figure 2.2f shows the corrected data from step 2. The reduced χ^2 for the linear fit is 1.085.

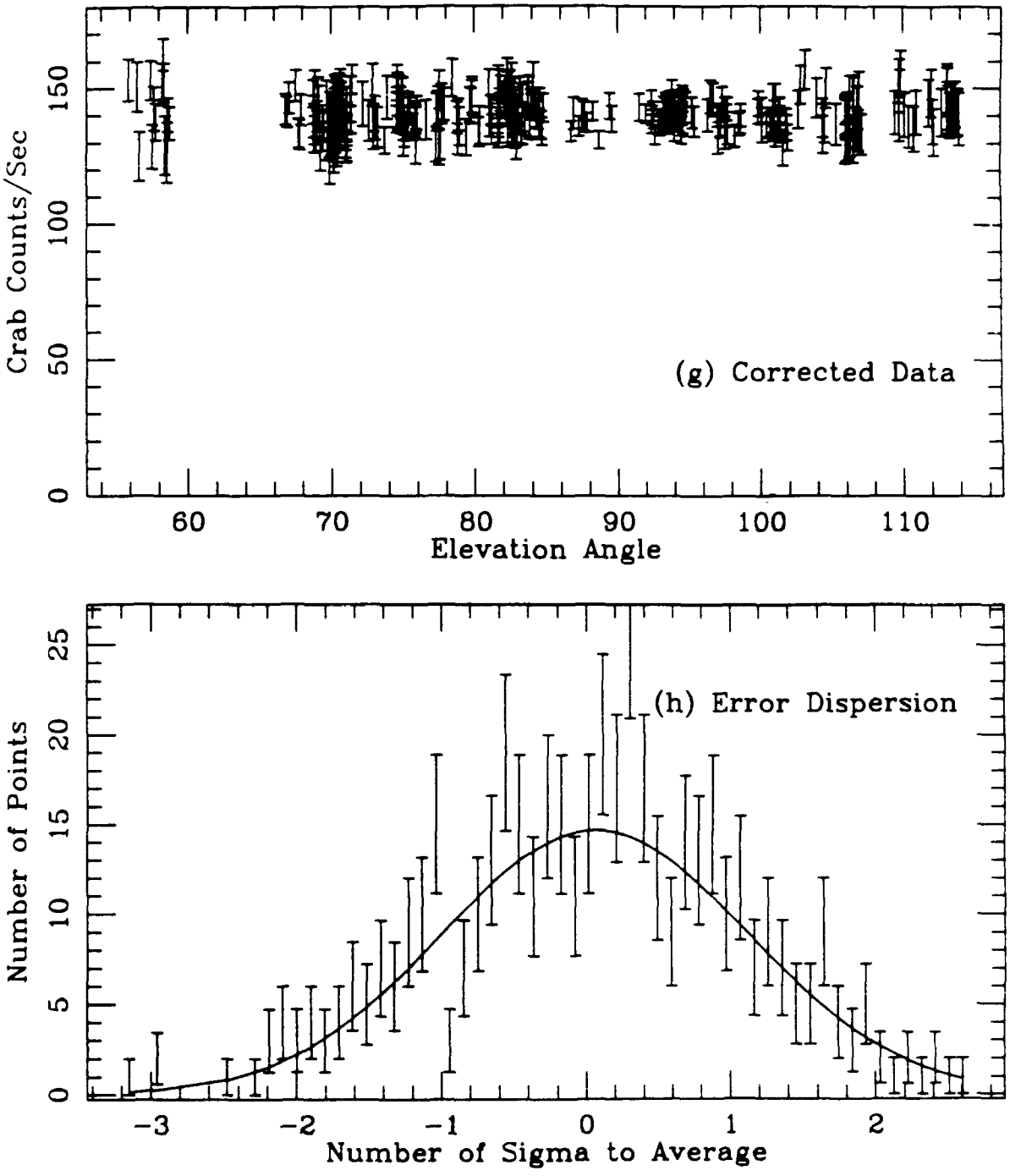

Figure 2.2: (g) The corrected intensity fits with error bars.
(h) The error dispersion. The curve is the minimum χ^2 fit to a Gaussian.

We now construct the angular response function which we normalize by the average intensity to make it independent of source. For each elevation angle θ, we associate a correction factor $f(\theta)$ given by

$$f(\theta) = a + b\theta + c\theta^2 + d\theta^3$$
$$I_0'' = I_0' f(\theta)$$
$$\sigma'' = \sigma' f(\theta) \qquad (2.2.3)$$

where I_0' and σ' are the results from section 5 above. We now apply our new response function to the pre-polynomial fit data. The reduced χ^2 is 1.08 (446 d.o.f.) and the new data is shown in figure 2.2g.

For completeness, the following table summarizes the results of this section (note: all coefficients are given for θ given in units of $-\pi/2 \le \theta \le \pi/2$.

Table 1

Channel Crab Correction Coefficients and Averages

Coefficient / Channel	a	b	c	d	avg
Center A	1.000	-0.084	-0.328	-0.615	140.369756
Center B	1.000	-0.131	0.131	-0.378	30.964078
Center C	1.002	-0.105	0.346	0.245	20.613074
Center D	2.165	-0.769	13.180	12.544	.694907
Left A	1.000	0.004	-0.383	-0.297	137.685564
Left B	1.001	0.122	0.101	-2.261	35.134279
Right A	1.000	0.058	-0.630	-0.701	141.724995
Right B	1.003	0.138	0.813	-1.089	22.635886

It should be noted that the result for the D channel is highly questionable due to the low source count rates and correspondingly large relative Poisson error.

7. Additional Systematic Error

The question of whether there should be additional error added to the Poisson error is a delicate one. Figure 2.2.h is a histogram of the number of center slat A points that are a given number of σ away from the average given in the table above. Superimposed over the histogram is a Gaussian fit. The fit has a reduced χ^2 of 0.898 which translates into a confidence of 68% and so is a fairly good fit. If the only source of error were Poisson fluctuation we would expect an approximate Gaussian. Since the distribution of error is nearly Gaussian we can conclude that the residual systematic errors are as small as, or smaller than, the Poisson error and therefore, to first order, negligible. The resulting data set seems to be as unbiased and Poissonian as possible and thus no further corrections are made. The net results from this analysis are:

1. We have determined a set of objective criteria through which to screen the data set.
2. We have written an elevation dependent response function based on real data which corrects for systematic defects in each of the channels.
3. We now have confidence in the corrected data set. Any morphology or periodicity observed in the data is likely to be true and not the result of some sort of processing artifact or systematic defect.

Chapter 3: Application to A0620

The attribution of errors to the data is the least certain part of the reduction scheme. There are systematic errors which may be as large or even larger than the Poisson errors associated with the count rate. In particular, the systematic detector defects due to elevation angle are a major subject to address. In chapter 2, I showed how the Crab Nebula was used to evaluate these systematic defects and correct for them. In this chapter I use these results in the analysis of the A0620 data.

A paramount concern is to retain as much data as possible without compromising our confidence in it. In this spirit, the following eight-step process was used. Figure 3.2 illustrates each step as carried out on the center slat A detector (1.3 - 5 keV). Figure 3.3 shows the final results for the A and B detectors.

1. Extract as much data as possible from rise.

One of the most interesting sections of data was that obtained during the initial rapid rise in the intensity from background to peak intensity immediately after the discovery of A0620. Unfortunately, the position of A0620 was initially not known to a high degree of accuracy. In the rush to locate and identify the source, many satellite aspect changes were made and as a result, it is difficult to derive accurate position data. There are two major errors: timing errors, and changes in the spin rate *during* a source scan.

A timing error occurs if the source is not in the field of view when the *aspect* program predicts that it will be. Small timing errors, on the order of a second, are easily corrected (see chapter 2.1). Large timing errors, on the order of tens of seconds, are more difficult to correct. There may be several

sources in the scan, but we are required to pick the correct source. This is difficult late in the decay phase of the nova, however in the early part of the light curve, especially during the rise, A0620 is much brighter than anything else in the X-ray sky (on the order of 500 Crabs!) We can therefore slide the *aspect* triangle response function "by hand" into the correct time interval and then carry out the fit described in 2.1 while maintaining a high degree of confidence in the data.

Dealing with spin rates that are changing during the source scan is not so simple. First, the light curve is no longer a triangle as shown in figure 3.1. Second, frequently the spin information is not contained in the orbital information data files and *aspect* uses the wrong spin rate. This results in triangle response functions with the wrong base width (fig 3.1).

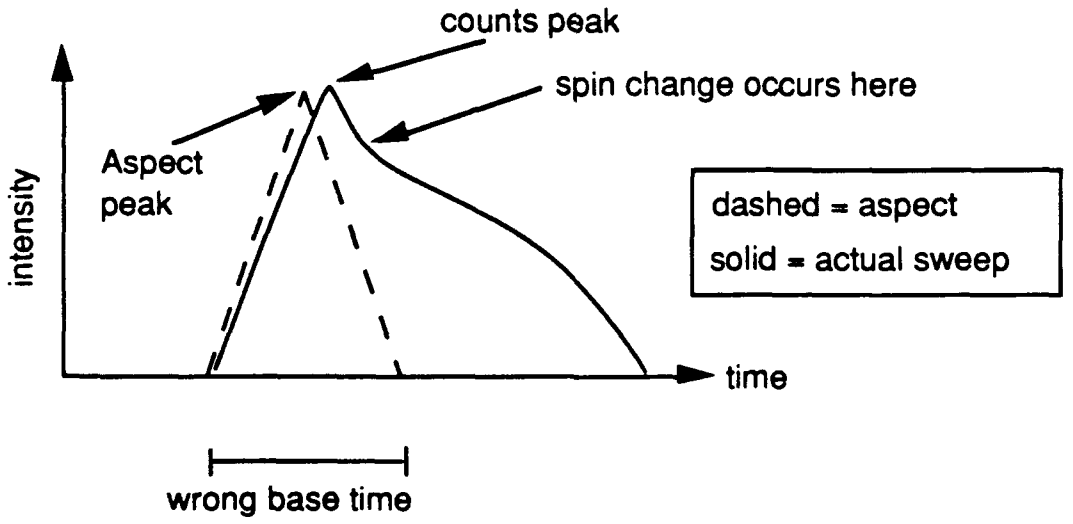

Figure 3.1: Spin rate change during a source scan. The source scan is much wider than the *aspect* prediction. Also the shape is not triangular.

In an attempt to recover data afflicted by these problems, we assume that the elevation information is correct and use the peak of the aspect curve with the peak of the counts to obtain the intensity according to the formula

$$I = \frac{\text{peak counts - average background}}{\text{peak transmission function}} \qquad (3.1)$$

where the average background is obtained by examining the data on either side of the scan. We associate Poisson errors with each of these points in the usual fashion

$$\sigma = \frac{\sqrt{\text{peak counts + avg background}}}{\text{peak transmission function}} \qquad (3.2)$$

Empirically, these points agree well with the other data points generated by the fitting so we maintain a high degree of confidence in the data quality. Figure 3.2a shows raw data and 3.2b shows the same data with a corrected rise time.

2. Eliminating Data Contaminated by X-rays from the Crab Nebula

The slat detectors have a very large field of view (2°x70° FWHM for the center, 1°x70° for the left and right slats). Other sources may be in the field of view at the same time as A0620 and affect the intensity fitting. The only source of consequence near A0620 (RA 95.0°, DEC 0.0°) is the Crab Nebula (RA 82.9°, DEC 22.0°). It so happens that on rare occasions both sources are in the field of view at the same time. When this happens, we find the percentage overlap of the triangle response functions and multiply this by the average crab intensity for that detector (average intensity

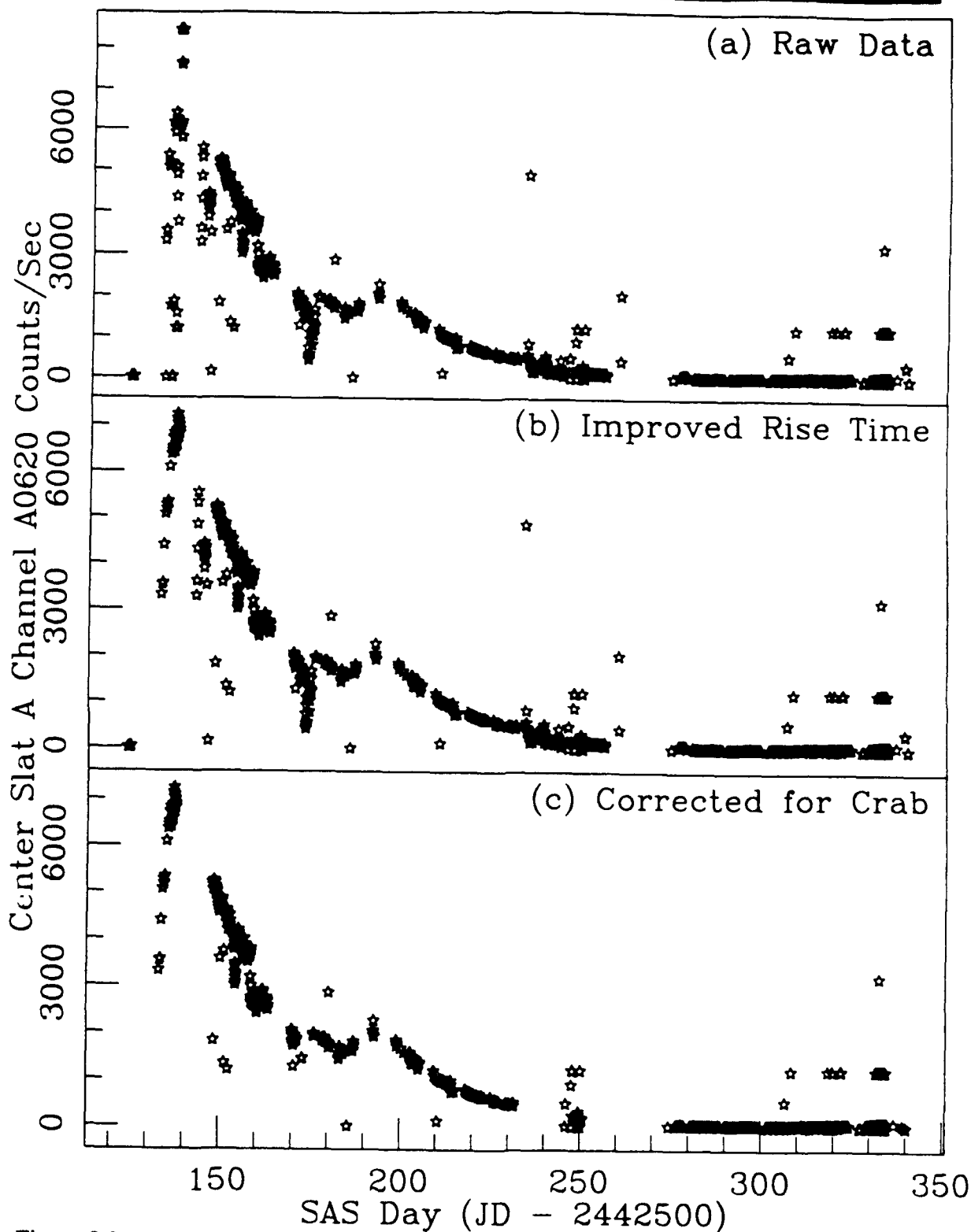

Figure 3.2: (a) Unprocessed intensity fits.
(b) Data after improvement of the initial rise.
(c) After eliminating data contaminated by the Crab Nebula.

determined in Chapter 2.2). We then subtract these counts from the measured counts of A0620 and these are our new counts. Intensities and Poisson errors are then calculated in the usual fashion using these new counts. Again, the corrected data tracks well with the untainted data and so we retain a high degree of confidence in our correction algorithm. The purified data are shown in 3.2c.

3. Full Width at Half Maximum

According to the description of the instrumentation on SAS-3 (Taylor, 1975) the FWHM of the slat detectors is ± 35°. From the observations of the Crab Nebula (Chapter 2), I find that outside this range the data cannot be corrected reliably. Therefore I remove all data outside the FWHM. Figure 3.2d shows the corrected data for the center slat A channel.

4. Remove Timing Errors

Next we remove data with timing discrepancies greater that ±8.64 seconds (10^{-4} days). In analyzing the initial rapid rise we expended a great deal of effort to use even this type of data. However, as the nova's intensity exponentially decays, it becomes harder and harder to discern A0620 from other sources. Fortunately, there are not many scans that have excessive timing errors and we do not have to discard very many data points. Figure 3.2e shows discarded data as stars.

5. Other Problem Data

Data are discarded for several other reasons which were explained in more detail in Chapter 2. The following is a brief summary.

If the data come from a pointing mode observation, the scanning mode analysis package is no longer appropriate and the data are discarded. If the

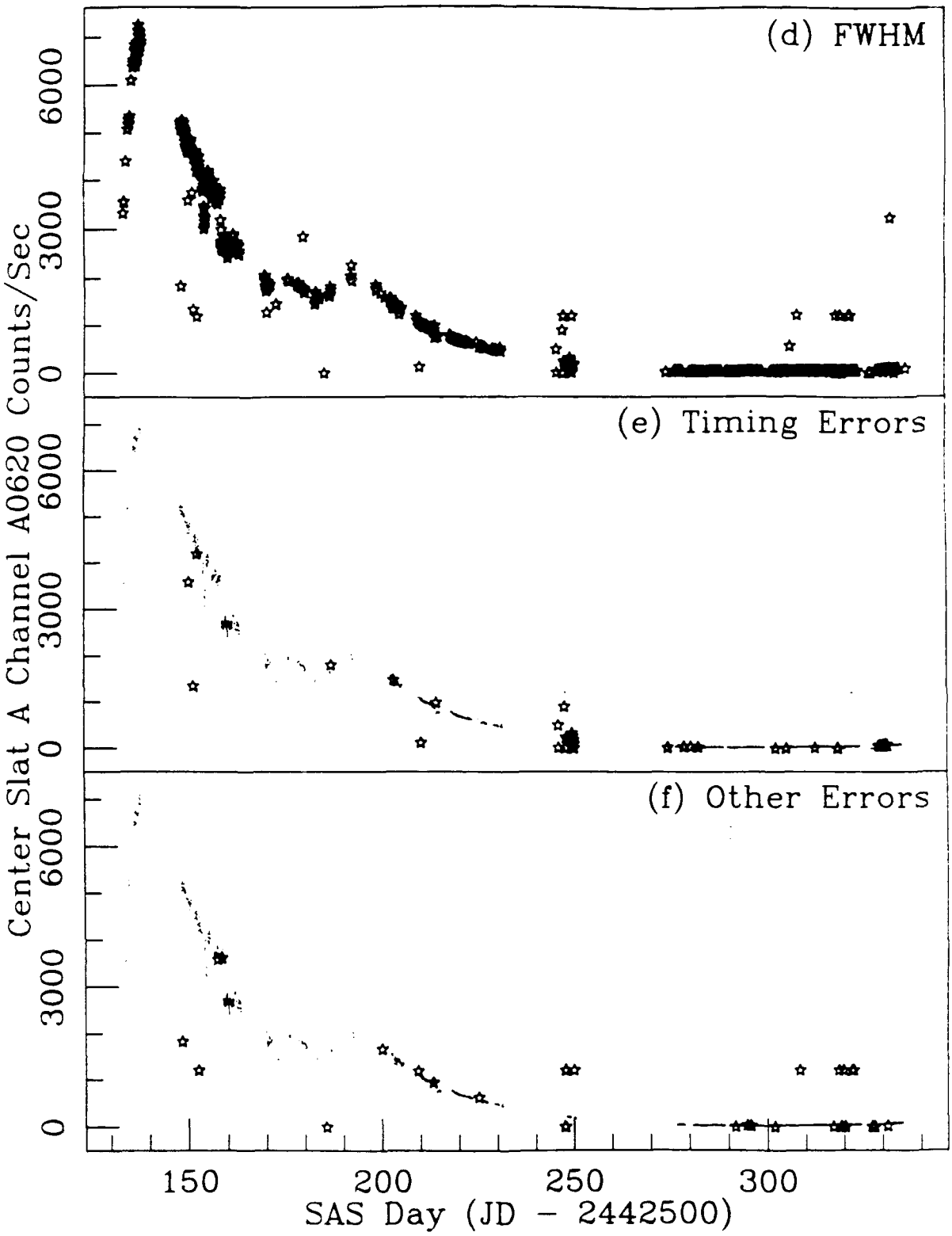

Figure 3.2: (d) The data after removing points obtained outside the FWHM.
(e) Points with timing errors shown as stars.
(f) Points with SNR < .5, σ/I_0 > .5 and not from scans depicted as stars.

data come from a scan with a very high spin rate, we find (from the Crab data) that it is also poorly fit, and must be discarded.

We also require that the signal to noise ratio be within acceptable limits (empirically 2 for A and B channels which have high count rates). For the C and D channels have such low count rates that this test is not appropriate. Finally, we require that the data be meaningful in that $\sigma/I_0 > .5$. We only require this of the A and B channel data, the C and D channels being so low that this criterion loses relevance. Figure 3.2f shows the data removed by these tests as stars.

6. Correct for Window Transmission Angle

As explained in Chapter 2, the beryllium window is a source of low energy X-ray absorption. Increased elevation angles, θ, correspond to effective window thicknesses increased by a factor of $\sec\theta$. From Woo(1991) we make the window correction using an average hydrogen column density of $N_H = 3.5 \times 10^{22}$ particles/cm^2 and an average spectral index of $\alpha = 6.43$. Figure 3.2g depicts the center slat A channel data after window correction.

7. Correct Systematic Errors Due to Elevation

In Chapter 2 I derived a systematic correction factor due to elevation for each detector. For each elevation angle, θ, there is associated a percentage correction $f(\theta)$. Figure 3.2h depicts center slat channel A after this correction is carried out.

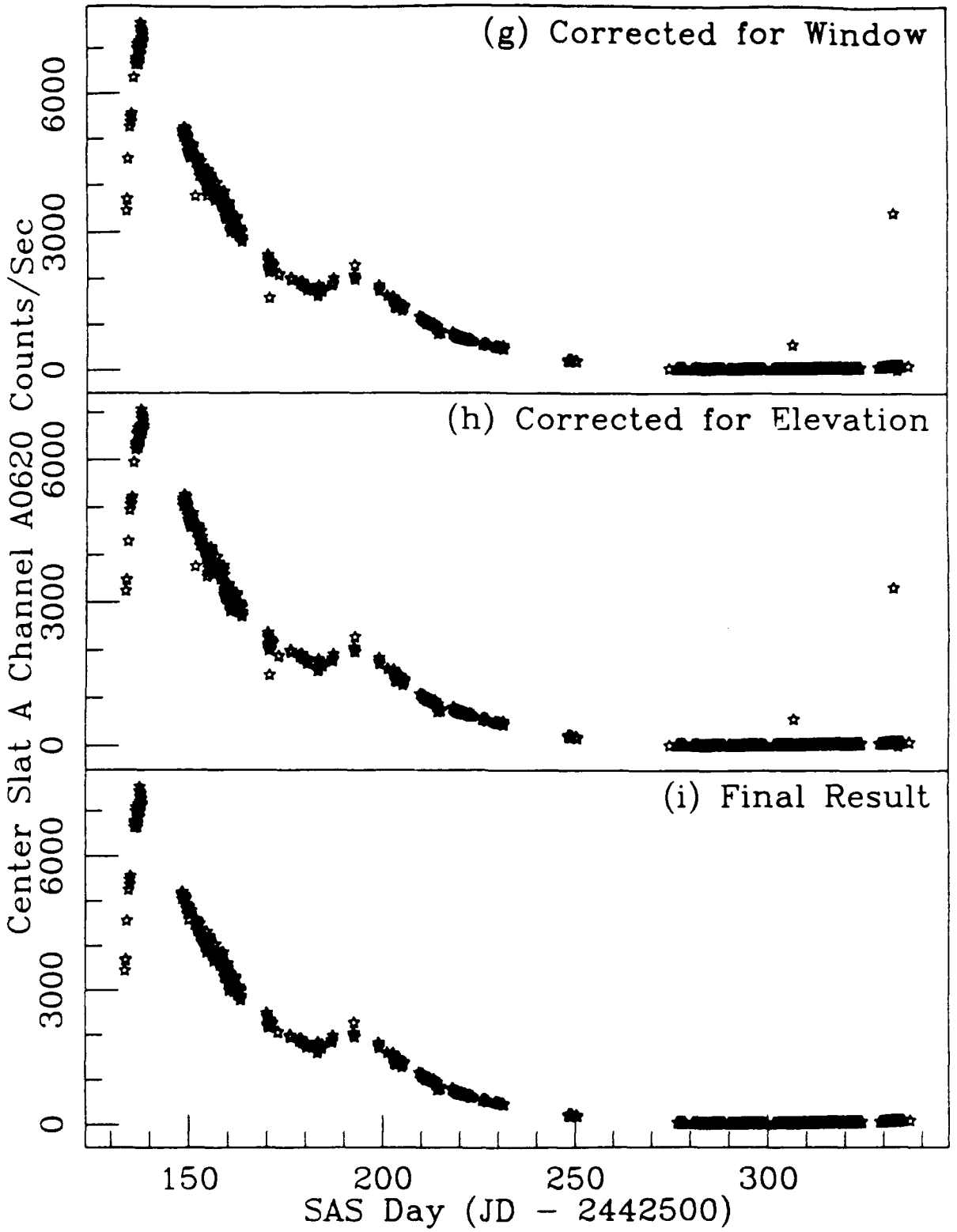

Figure 3.2: (g) Data after window correction.
(h) Data after elevation angle dependent response functions.
(i) The final data set. Note improvement over fig.2.2a.

8. Remove Excessive χ^2

Lastly we remove data points for which the reduced $\chi^2 > 3.0$. This removes points which were poorly fit by the fitting routine. We now have a high degree of confidence in the data set and any deviations from the norm are probably significant features of the data and not artifacts of the processing. The final light curve is shown in figure 3.2i and is quite an improvement on 3.2a.

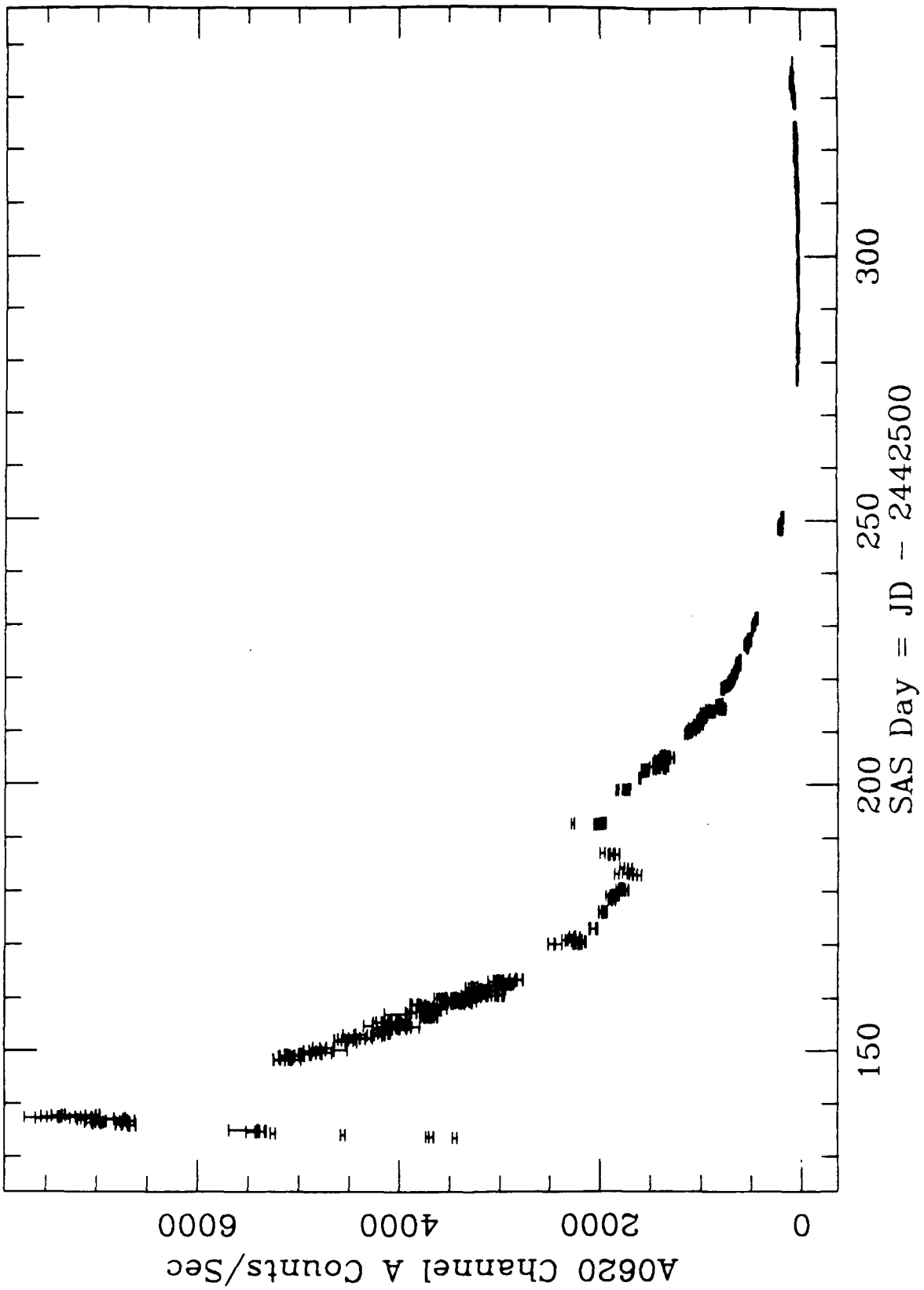

Figure 3.3: (a) The Center Slat A channel final data set.

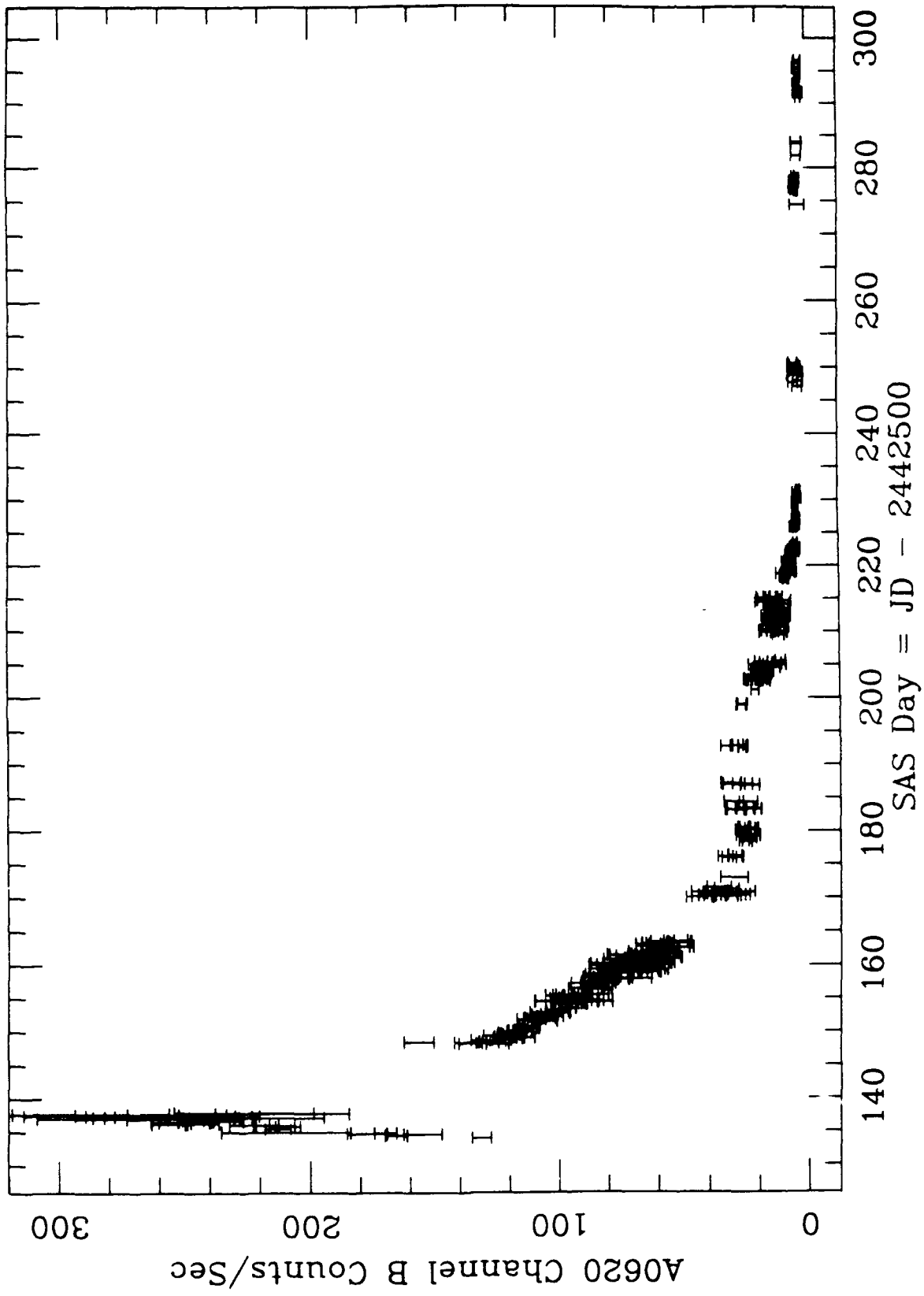

Figure 3.3: (b) The Center Slat B channel final data.

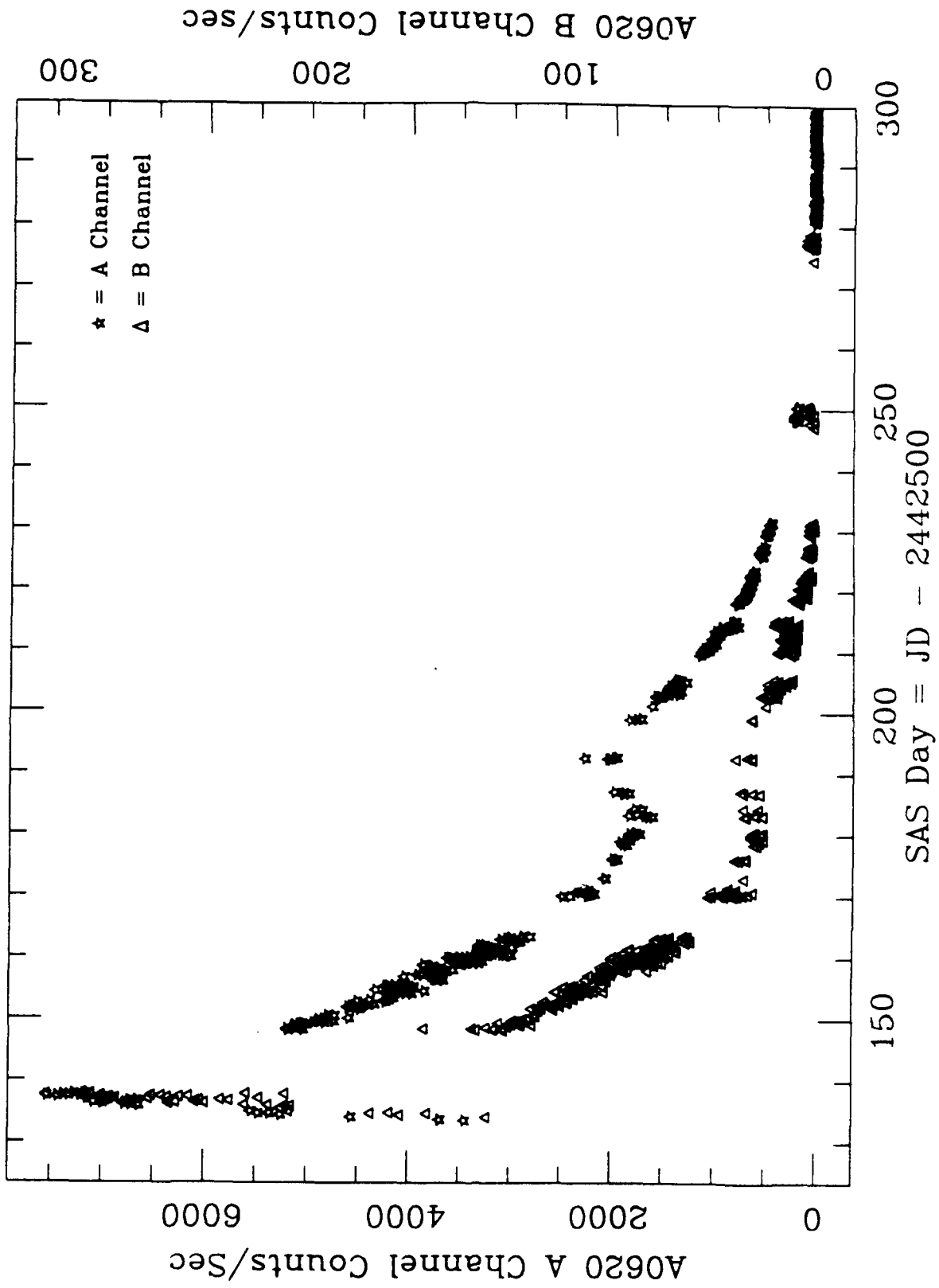

Figure 3.3: (c) Center Slat A and B channel plotted together.

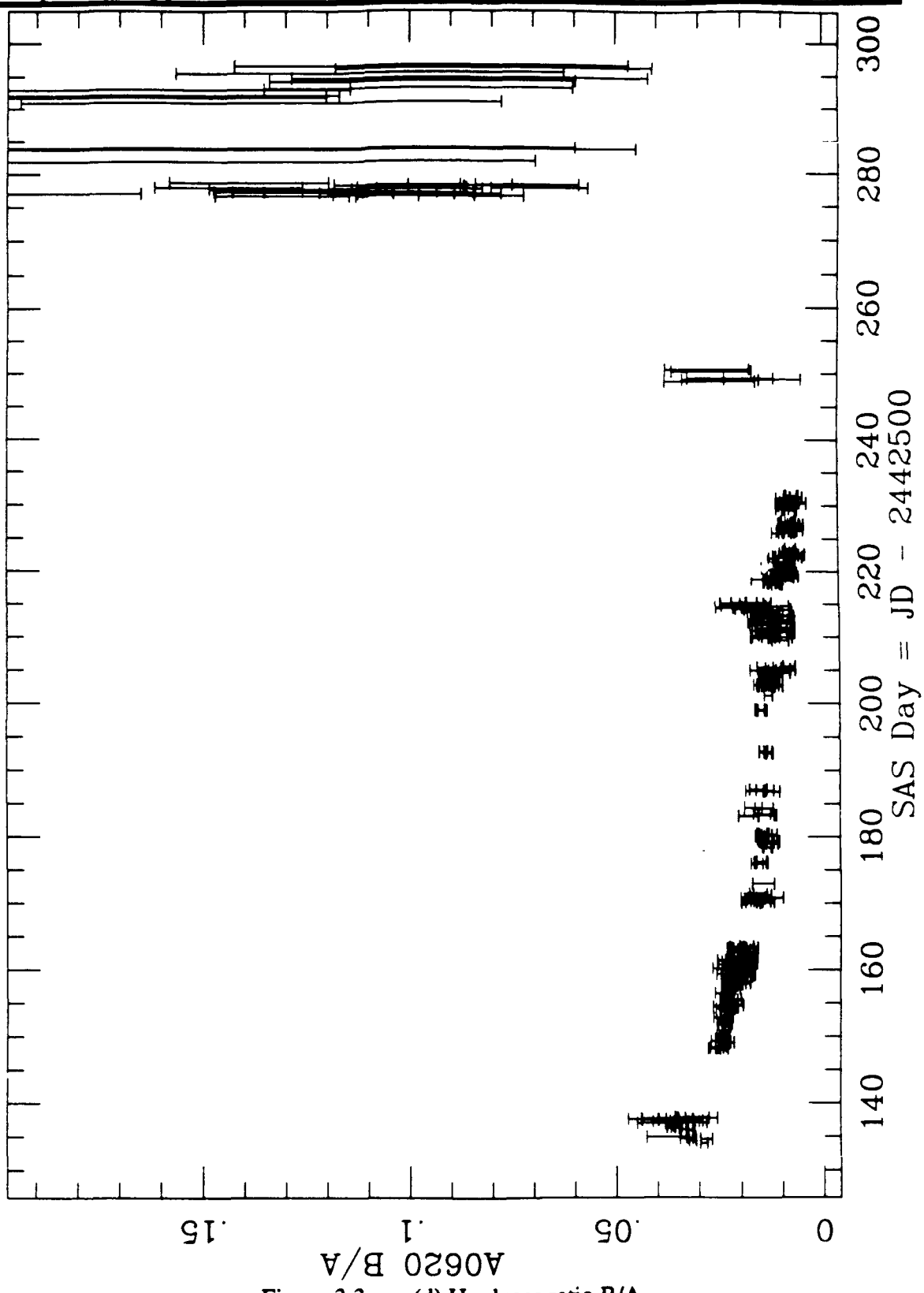

Figure 3.3: (d) Hardness ratio B/A.

Chapter 4: Data Analysis

After reducing the data, and attributing the proper error to each datum, we can proceed to extract the desired information about the presence of absence of periodicities. In particular, we are interested in whether there is evidence for the observed 7.75^h optical period found by MR. We also seek to confirm the 7.8^d X-ray period found by MB. The 7.8^d period is of particular interest since MB used the same data, but *without* the improved data reduction. We will show that the improved reduction yields a data set so "clean" that it allows us to place strict upper limits on the amplitude of oscillations

We examine the long term scanning mode data from the slat collimator detector by the method of phase dispersion minimization.

4.1 Phase Dispersion Minimization

The idea of phase dispersion minimization is to fold the data at all possible periods, Π, within the range Π_{min} to Π_{max}. Following Stellingwerf(1978) we define the variance to be

$$\sigma^2 = \frac{\Sigma(x_i - \overline{x})^2}{N-1} \qquad (4.1.1)$$

where the sum is from 1 to N, x_i is the i^{th} datum and we have a total of N data points. For any subset, or bin, of $\{x_i\}$ we define the sample variance s^2 exactly as in (4.1.1) except that N is replaced by n, the number of elements in the subset.

Suppose that we have M subsets such that the variance of the j^{th} subset is s_j^2 and the number of elements in it is n_j. We define the overall variance for all of the subsets to be

$$s^2 = \frac{\Sigma(n_j - 1)s_j^2}{\Sigma n_j - M} \tag{4.1.2}$$

Suppose that we choose these subsets to be phase bins. Choose a period Π and assign each x_i to a phase $\phi_i = t_i \bmod(\Pi)$ where t_i is the time of measurement x_i. Then we can divide the set $\{x\}$ into M bins where all the members of bin j have similar ϕ_i. Define the statistic

$$\Theta = s^2/\sigma^2. \tag{4.1.3}$$

If we have chosen the correct period, then s^2 will be very small compared to neighboring periods and Θ will be a local minimum. If Π is not the true period then $s^2 \approx \sigma^2$ and $\Theta \approx 1$. We therefore seek to minimize Θ.

In practice we pick N_c covers on N_b bins for a total of $M = N_c N_b$ subsets. We then add these subsets into N_b bins of width N_c.

To analyze the statistical certitude of any observed periodicity we follow Stellingwerf(1978) and note that Θ is the ratio of the variances of two subsets of the data set, that of the total set and that of the bins, and therefore obeys an F distribution with $\Sigma n_j - M$ and N - 1 degrees of freedom. It is convenient to have $F > 1$ so define $F = \Theta^{-1}$ when $\Theta < 1$ and $F = \Theta$ otherwise. For convenience, I will assume that $\Theta < 1$ (if $\Theta > 1$ replace Θ by Θ^{-1}).

We can apply the two-sided test to determine the probability, P, that a given value of Θ is due to random fluctuations. This "significance" is twice the area of the F distribution above Θ^{-1}. The significance P is given by

$$F_{(p/2,N-1,\ \Sigma n_j - M)} = 1/\Theta \tag{4.1.4}$$

we then find P by consulting an F table.

Stellingwerf points out that this can be simplified by noting that if N is large (>100) then the variance of our sample approaches the true population variance. In that case we can use the χ^2 test

$$\chi^2_{(p/2,N-1)} = (\Sigma n_j - M)\Theta \tag{4.1.5}$$

Now P is twice the area of the χ^2 distribution below $(\Sigma n_j - M)\Theta$.

The above discussion places no upper limit on periodicity amplitude. In chapter 4.2, I will discuss how to place upper limits on the periodicity amplitude using the observed value of Θ.

Since the data are rapidly decaying and are being sampled periodically, it is necessary to detrend the data. Failure to do so can cause false periods to appear and also cause the effects of sampling to grow so severe as to mask out any periodicity which may be in the data set (Remillard, 1990). To do this I subtract a decaying exponential function from the data and then normalize according to the formula

$$y_i' = \frac{y_i - I_1 e^{-t/\tau}}{I_1 e^{-t/\tau}} \tag{4.1.6}$$

where y_i is the data point at time t, and I_1 and τ are the least squares fit parameters for the data set. This removes the long term trend in the data and allows us to examine departures from the mean value, and to search for periodicity.

In Chapter 4.2, I will apply these techniques to the A0620 data set in order to derive limits on the X-ray periodicity.

4.2 Results

In Chapter 4.1 we discussed the development of methods for analyzing the data. In this chapter we apply those methods to data from the A and B channels of the slat collimator detectors. We chose these channels because they provided the largest data sets (i.e. the most points). We also examine the hardness ratio B/A. In section 4.2.1, we detrend the data in preparation for the analysis. In section 4.2.2, we describe the Monte Carlo simulation we performed to analyze the data and present our results. In chapter 4.2.3, we confirm MB's data and examine their 7.8^{d} period claim.

4.2.1 Detrending the Data

We detrend the center slat A channel decay data as follows. We ignore the initial burst. We fit the initial decay from SAS day 137 to 175 with an exponential. We ignore the "hump" between SAS days 175 and 200 and then fit another exponential to the decay from SAS day 200 to 260. Since we are looking for periodic deviations from the mean and not singular events, we also remove the hardness "flare" at SAS day ~ 215. We concatenate the two fits together for periodicity searches and we name this section of the data the decay phase. Figures 4.2.1a-c show this process for the A channel where the curves represent fits and the error bars represent the data and uncertainty.

Detrending the final ramp phase of the data is difficult. There are few natural breaking points by which to change models and our breaking points are admittedly rather arbitrary. We detrended the data from SAS day 275 to 285 by fitting a line to it. We remove the average of the data between days

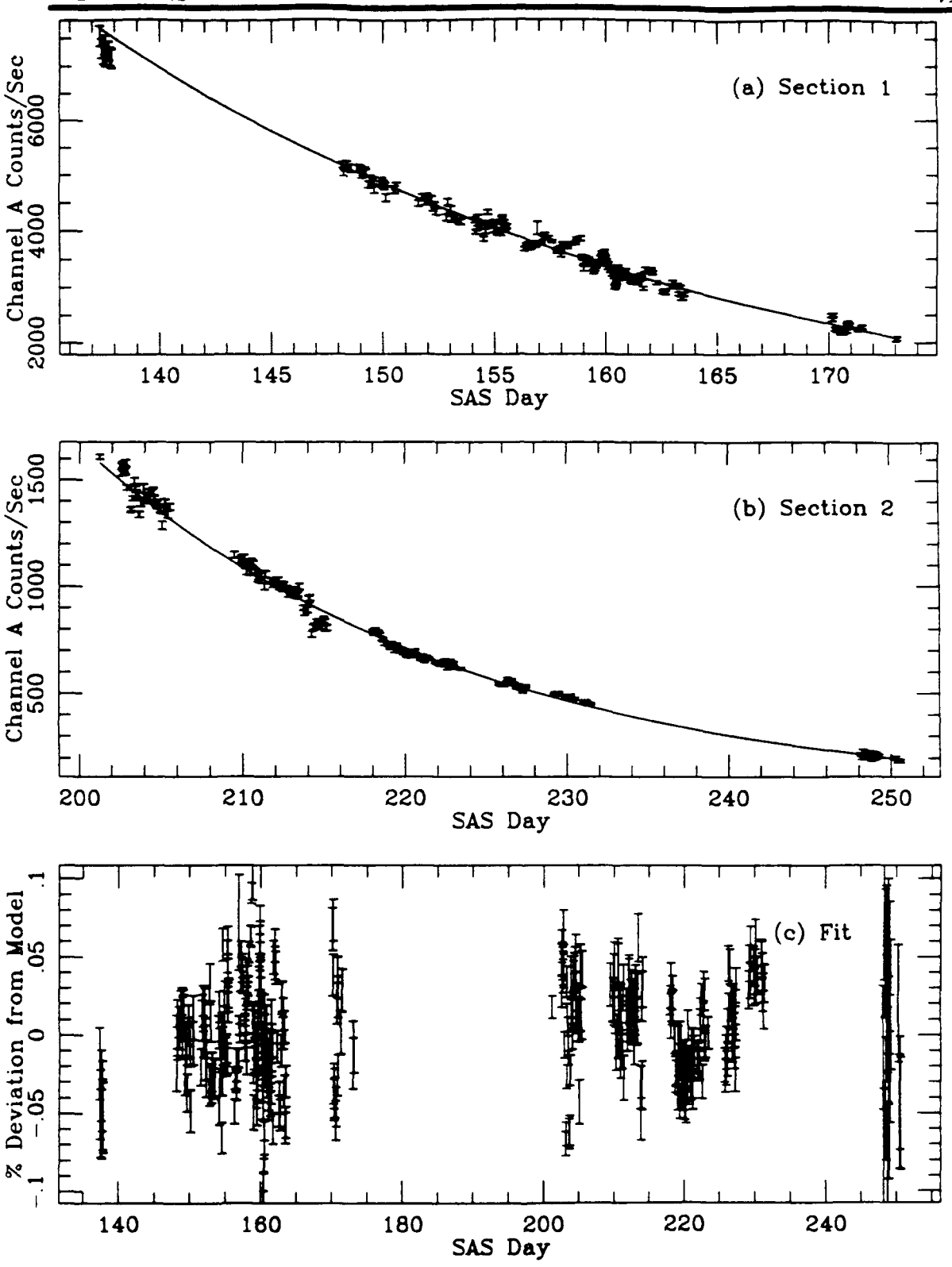

Figure 4.2.1: (a) Channel A fit for SAS days 137 - 175. Curve is best fit exponential.
(b) Channel A fit for SAS days 200 - 255. Curve is best fit exponential
(c) Combined percent deviations from models.

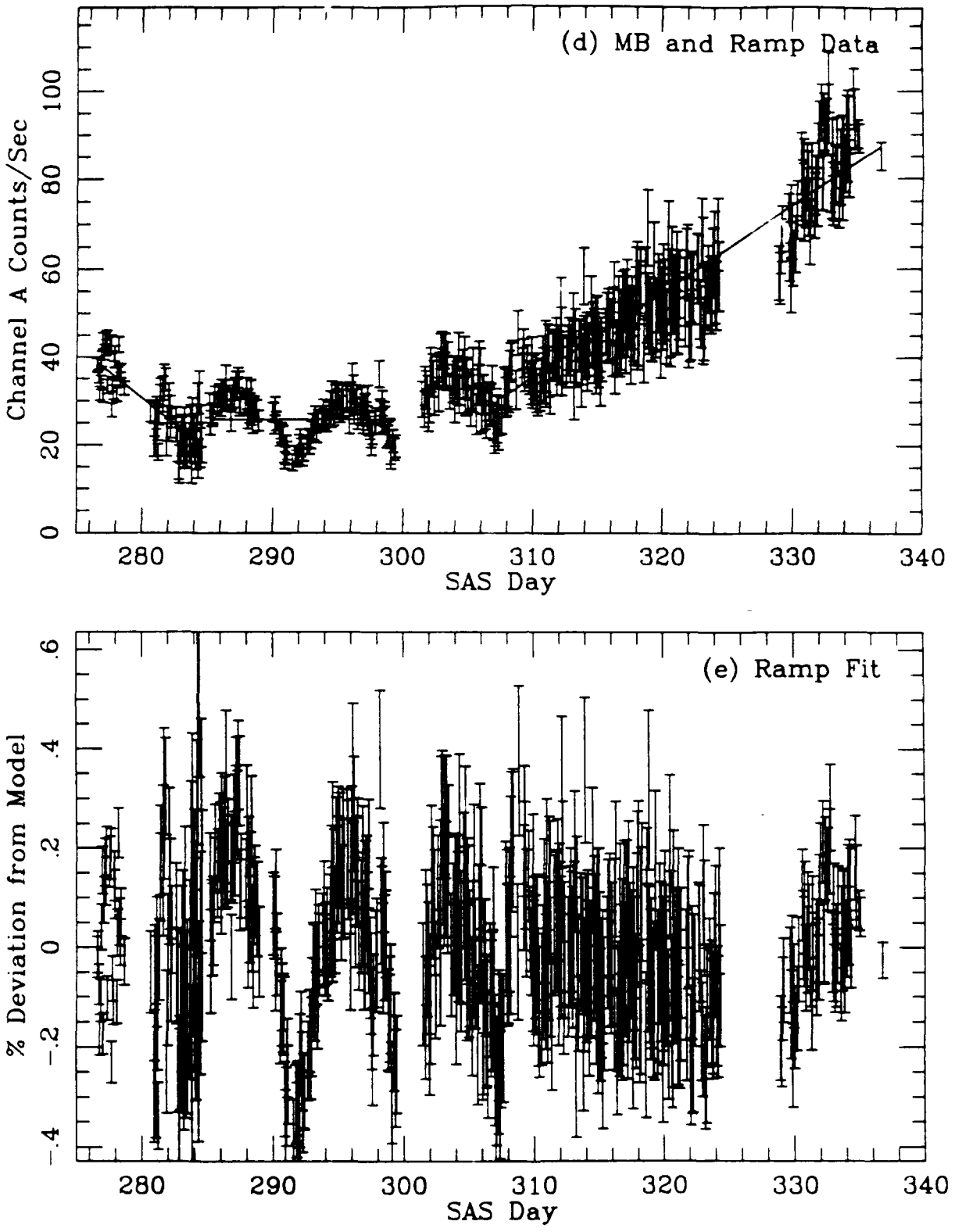

Figure 4.2.1: (d) Channel A fit for SAS days 275 - 340. Curves are best fits as described in text.
(e) Combined percent deviations from models.

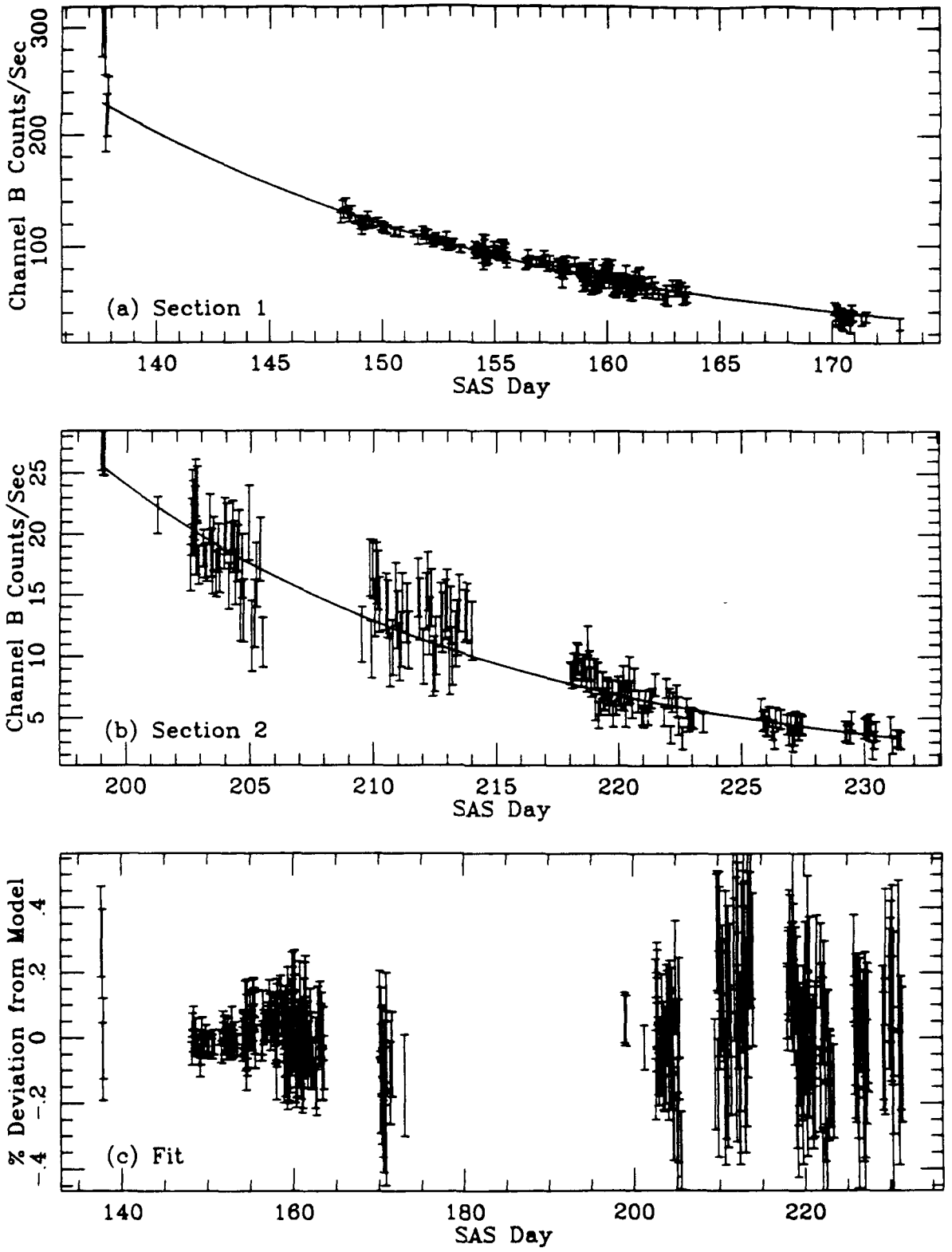

Figure 4.2.2: (a) Channel B fit for SAS days 137 - 175. Curve is best fit exponential.
(b) Channel B fit for SAS days 200 - 255. Curve is best fit exponential
(c) Combined percent deviations from models.

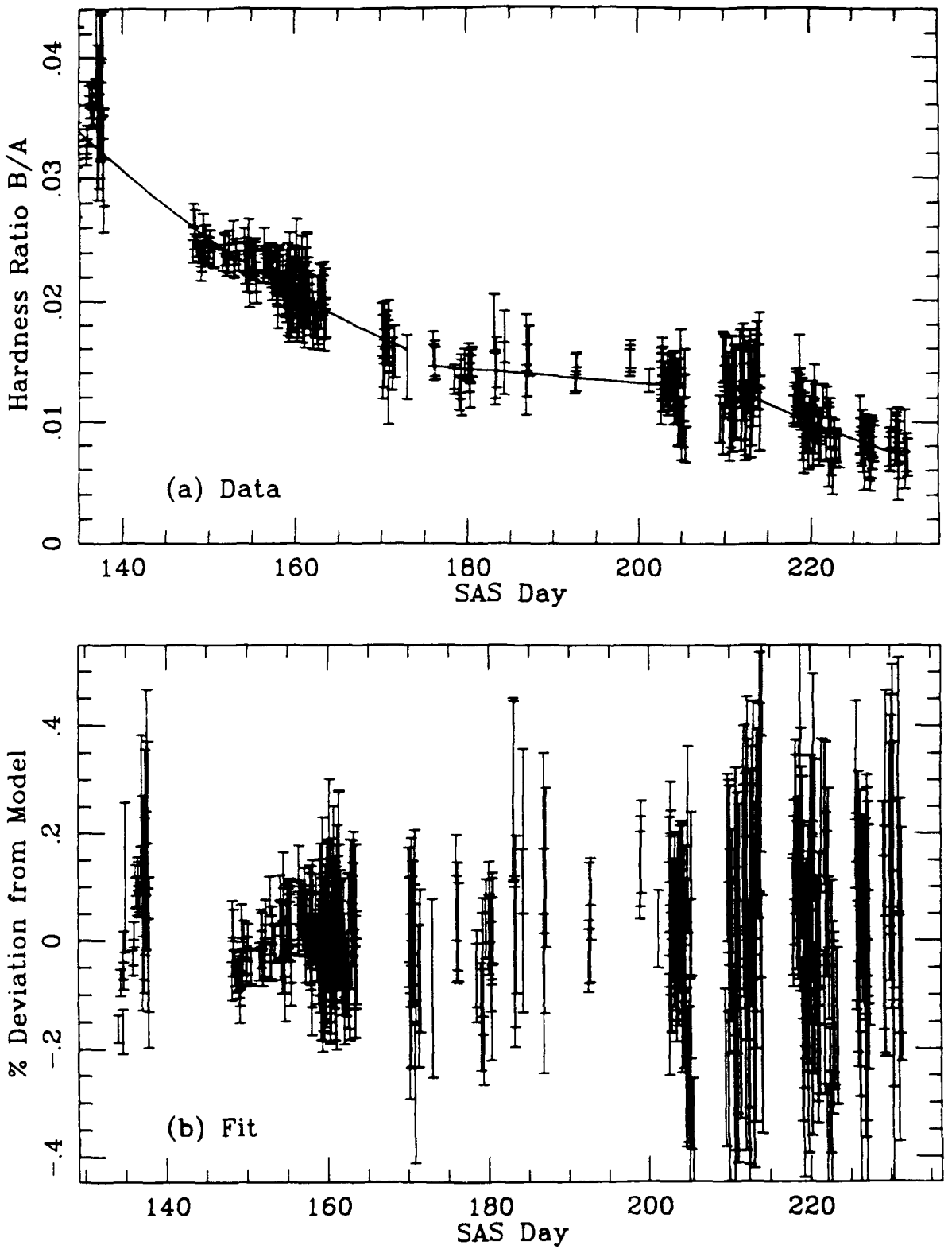

Figure 4.2.3: (a) Hardness ratio fit for SAS days 135 - 240. Curves are best fits.
(b) Combined percent deviations from models.

285 and 300 and between 301 and 307. We then fit the remaining data from day 208 to 338 by a line. Figure 4.2.1d shows the fits as curves and the data uncertainty as error bars. Figure 4.2.2e shows the resultant percent deviation from the model. In the analysis section, when we refer to the "ramp", "MB" and "improved MB" sections of the data we will be referring to the sections from day 308 to 338, day 285 to 322, and day 275 to 308 respectively.

We detrend the center slat B channel in an analogous manner to the center slat A channel and we show the results in figure 4.2.2. As before, the curve represents the model and the error bars represent the data uncertainties. We do not fit the B channel after SAS day 240 since it is at the background level and is no longer informative.

We detrend the hardness ratio B/A by fitting with an exponential between SAS days 137 - 175, a line from day 175 - 207 and another exponential from day 207 - 232. After this time the B channel is in the background and the hardness ratio is meaningless. Figure 4.2.3 illustrates the hardness fitting and figure 4.2.4 shows confidence contours for all of the exponential fits in parameter space. The confidence contours drawn are 99%, 95%, 90%, 68.3% and 10%. Table 2 tabulates the above fits.

TABLE 2a

Decay Fit Parameters

Det./Day[1]	τ [d^{-1}][2]	σ_τ [d^{-1}]	I_0[cnt/sec][3]	σ_I[cnt/sec]	Red. χ^2	dof
A/137-175	27.49	0.11	7768	25	11.4	206
A/200-260	23.52	0.05	1666	3.0	8.42	215
B/137-175	18.76	0.25	237.6	3.0	1.18	226
B/198-240	16.06	0.30	27.16	0.55	1.31	179
H/137-175	50.27	1.0	0.03736	0.0031	1.84	226
H/175-207	-5.67E-5	0.02E-5	0.01460	0.0	1.06	76
H/207-232	34.29	5.3	0.01443	0.0011	1.18	140

1. A, B, and H refer to Center Slat A, Center Slat B and B/A respectively. Days are SAS days = JD - 2442500
2. For H 175-207 the time constant is the slope of the line.
3. For H 175-207 I_0 is the y-intercept of the line.

TABLE 2b

Ramp & MB Fit Parameters

Day[1]	m [d^{-1}]	σ_m[d^{-1}]	I_0[cnt/sec]	σ_I[cnt/sec]	Red. χ^2	dof
275-285	-2.388	0.11	38.86	0.15	4.25	71
285-300	N/A	N/A	25.79	0.36	4.32	153
300-307	N/A	N/A	32.74	0.26	1.37	68
308-338	1.941	0.05	31.02	0.36	0.96	248

1. Days are SAS days = JD - 2442500.

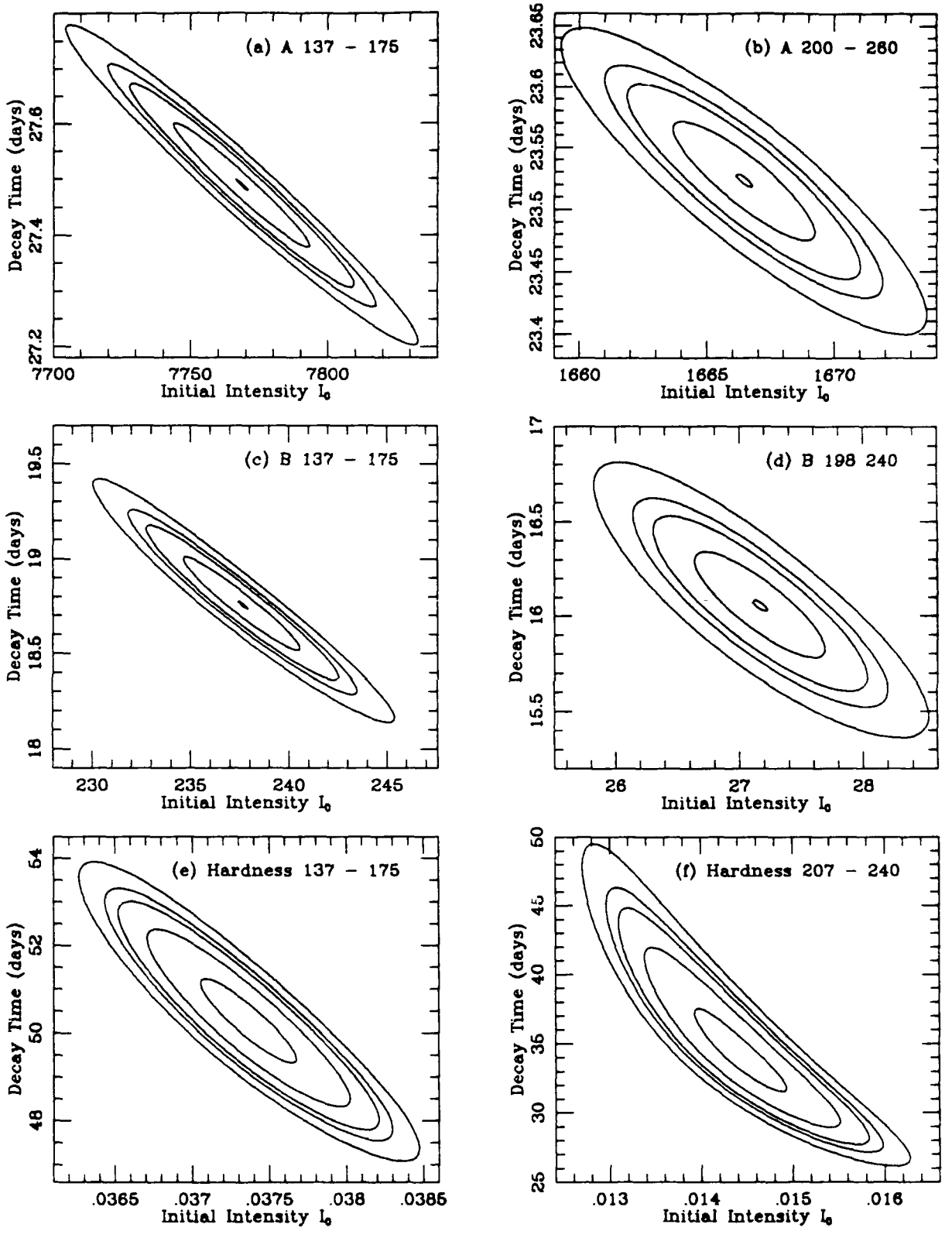

Figure 4.2.4: Confidence contours in χ^2 space for the various exponential fits. Labels denote channel and day range of fit. A = A channel, B = B channel and H = hardness ratio.

We now apply the techniques of chapter 4.1 to the slat collimator and the hardness ratio. Stellingwerf (1978) recommends using 5 bins with 2 covers to uncover periodicity. This binning strategy reduces side lobes and allows for rapid computation. If we see significant periodicity with this low resolution scan we can increase the number of bins and make smaller period steps to get a high resolution cut at the data. We perform the analysis for the various channels in figures 4.2.5a-h using this strategy in the ranges 7.5^h - 8^h and 6^d - 9^d.

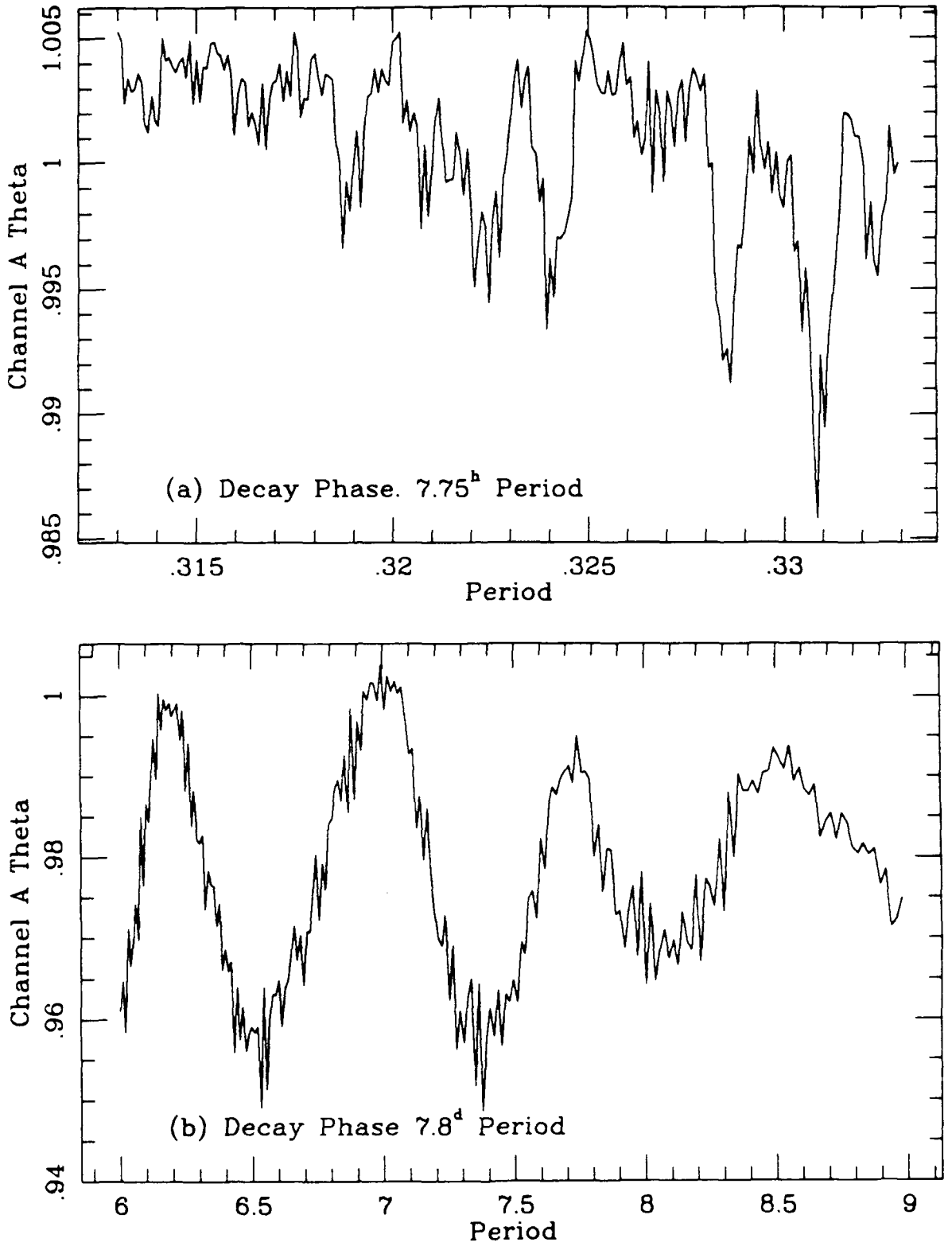

Figure 4.2.5: (a) Stellingwerf procedure on channel A decay phase at $\Pi = 7.75^h$.
(b) Stellingwerf procedure on channel A decay phase at $\Pi = 7.8^d$.

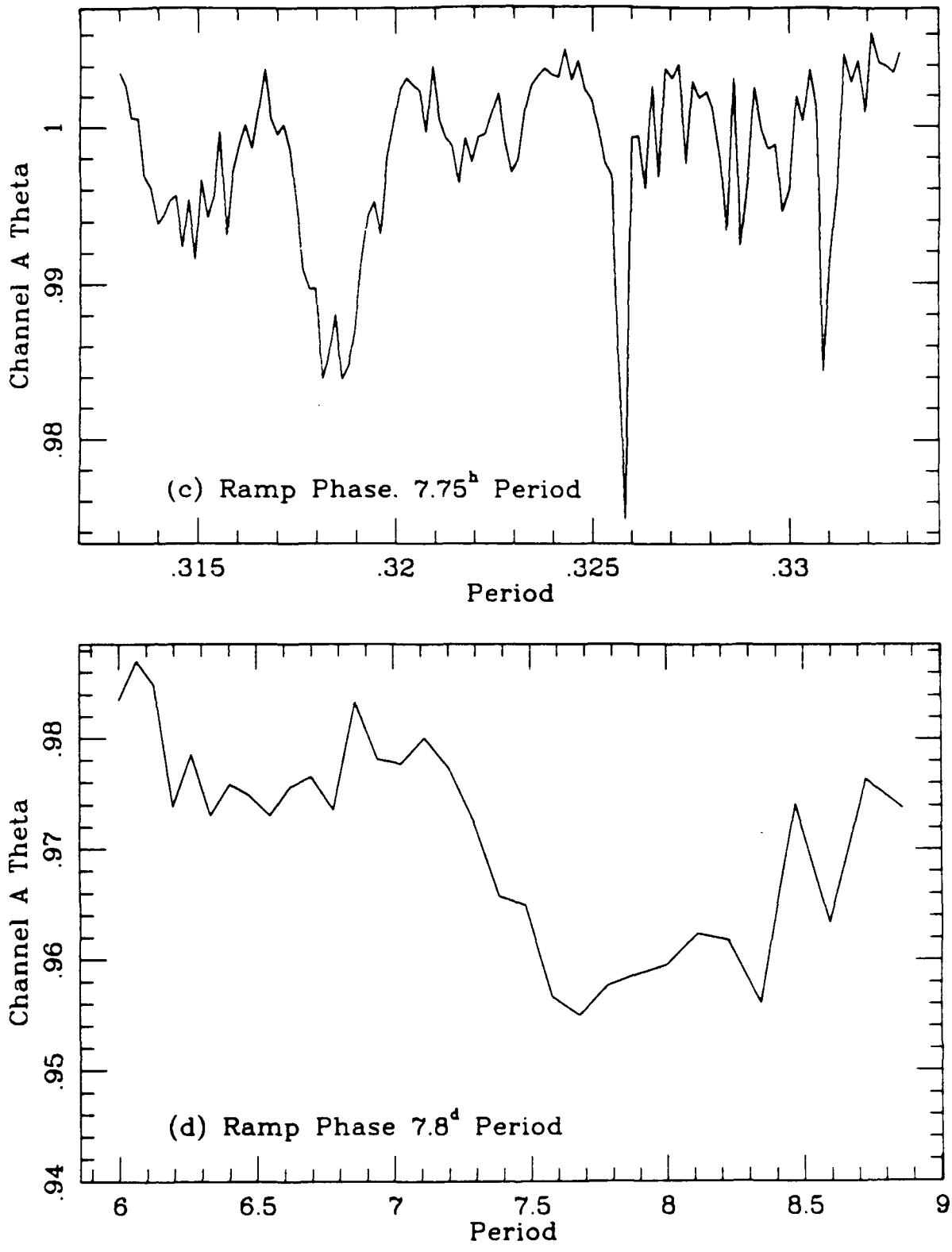

Figure 4.2.5: (c) Stellingwerf procedure on channel A ramp phase at $\Pi = 7.75^h$.
(d) Stellingwerf procedure on channel A ramp phase at $\Pi = 7.8^d$.

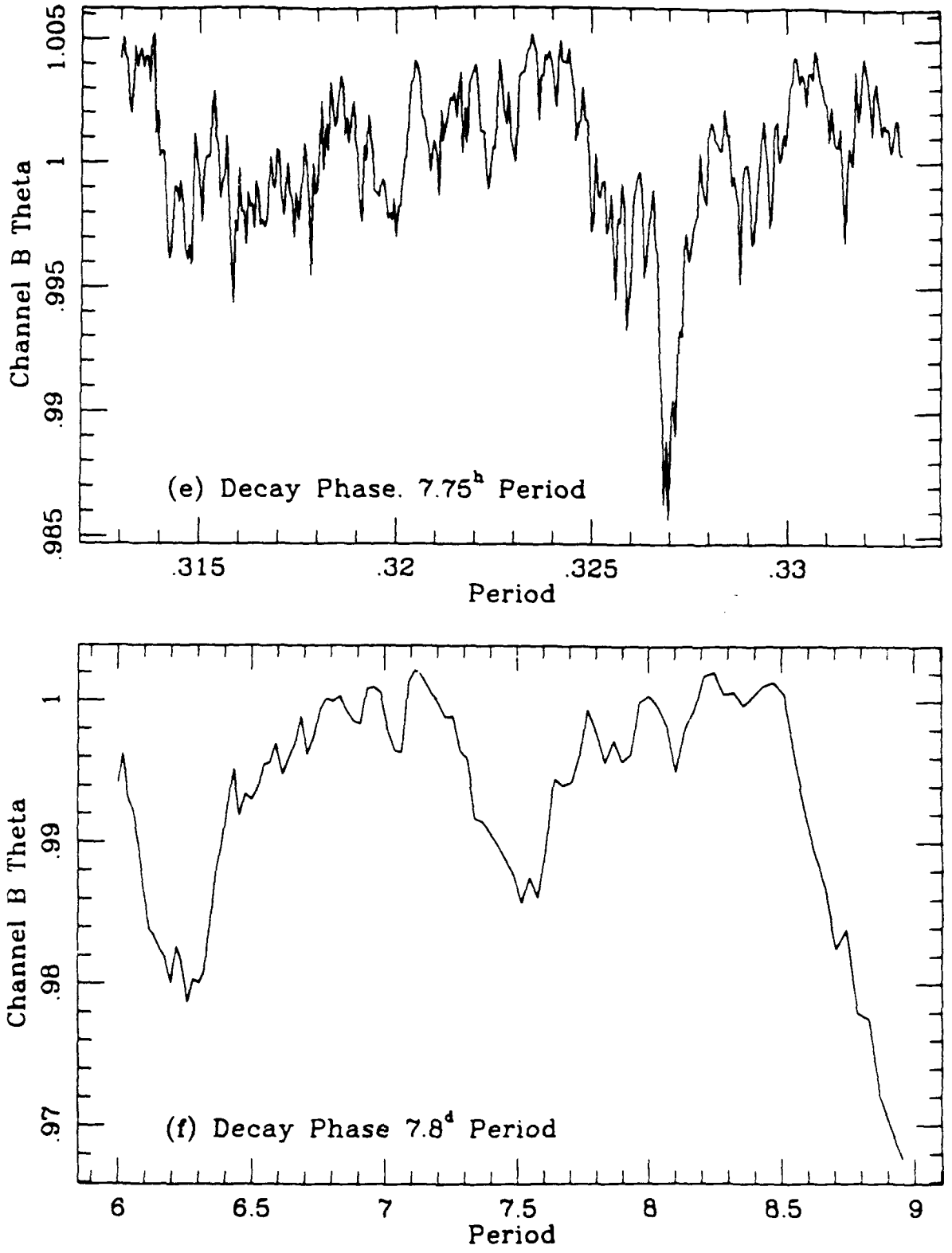

Figure 4.2.5: (e) Stellingwerf procedure on channel B decay phase at $\prod = 7.75^{h}$.
(f) Stellingwerf procedure on channel B decay phase at $\prod = 7.8^{d}$.

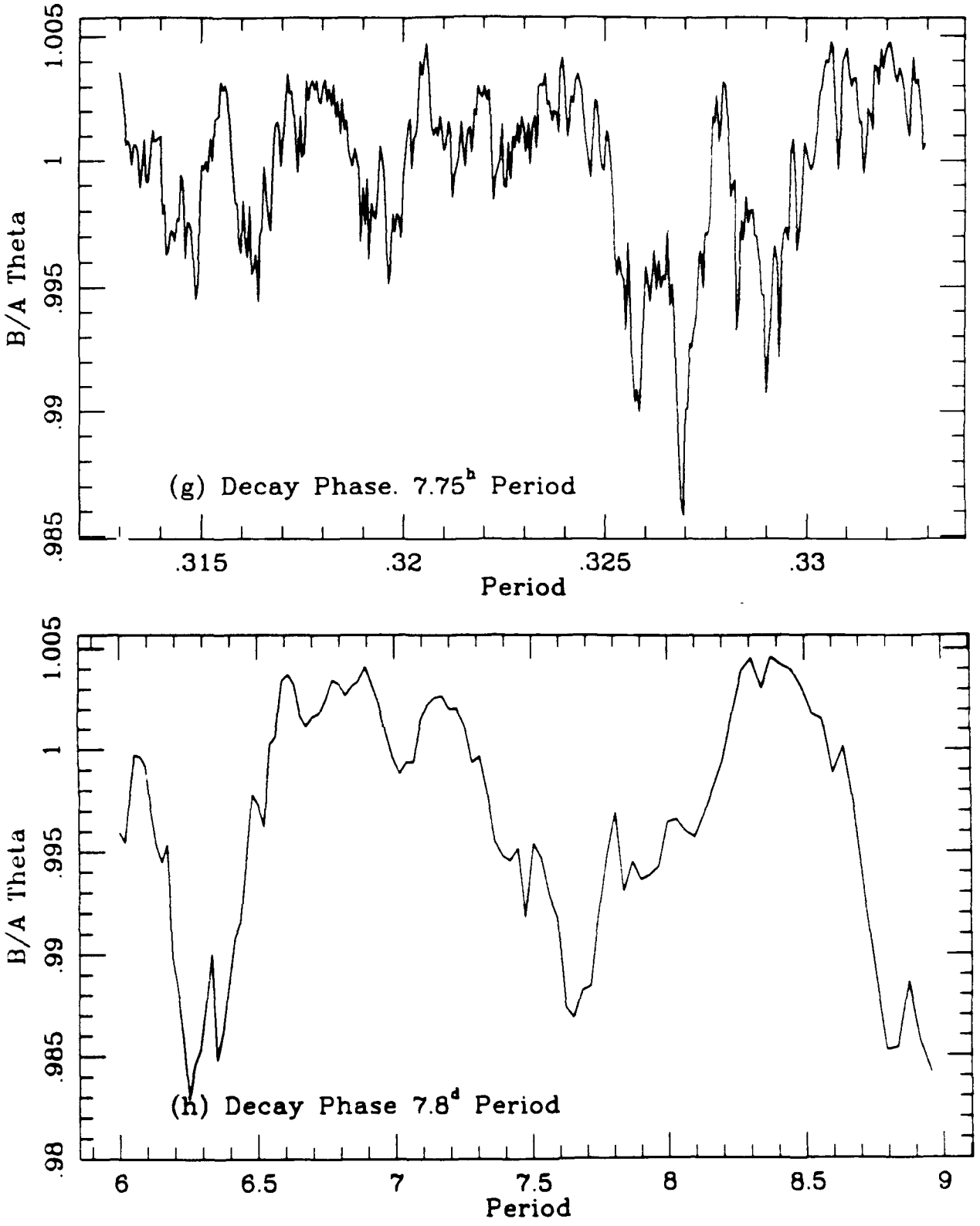

Figure 4.2.5: (g) Stellingwerf procedure on hardness ratio decay phase at $\prod = 7.75^{h}$.
(h) Stellingwerf procedure on hardness ratio decay phase at $\prod = 7.8^{d}$.

4.2.2 Monte Carlo Simulation

The values Θ obtained from figure 4.2.5 tend to support the hypothesis that the observed value of Θ is due to noise. To obtain an estimate of the upper limit on the periodic amplitude I conducted a Monte Carlo simulation.

We generated a thousand random data sets and calculate Θ at the period of interest for each set. To generate the data sets, for each data point we use the same time information as the original data set but place a Monte Carlo intensity in the place of the original intensity. We assume that the value of Θ obtained from the real data is as high as it is because of noise. The assumption that our data are pure noise gives us a worst case scenario because we are trying to show an absence of periodicity. Thus any bias in our simulation will favor periodicity and we err on the side of caution. Using this assumption, for each Monte Carlo intensity we generate random Gaussian noise with the same mean and deviation as the real data. On top of the noise, we add a sinusoid with the amplitude and period of interest. Figure 4.2.6a shows a sample of real data and 4.2.6b shows a sample of simulated data.

After generating the random data sets and calculating the corresponding Θ for each, we can make a histogram. Figure 4.2.7 depicts such histograms for the 7.75^h case for various period amplitudes, A. We define $T(\alpha)$ to be the number of simulations out of a thousand which yield a value of Θ as high as α or higher.

To generate upper limits on periodicity for a real data set, we use the value of Θ from table 3 (next page) and find the amplitude such that $T(\Theta)=3$ i.e. tne amplitude such that there is only three simulations out of a

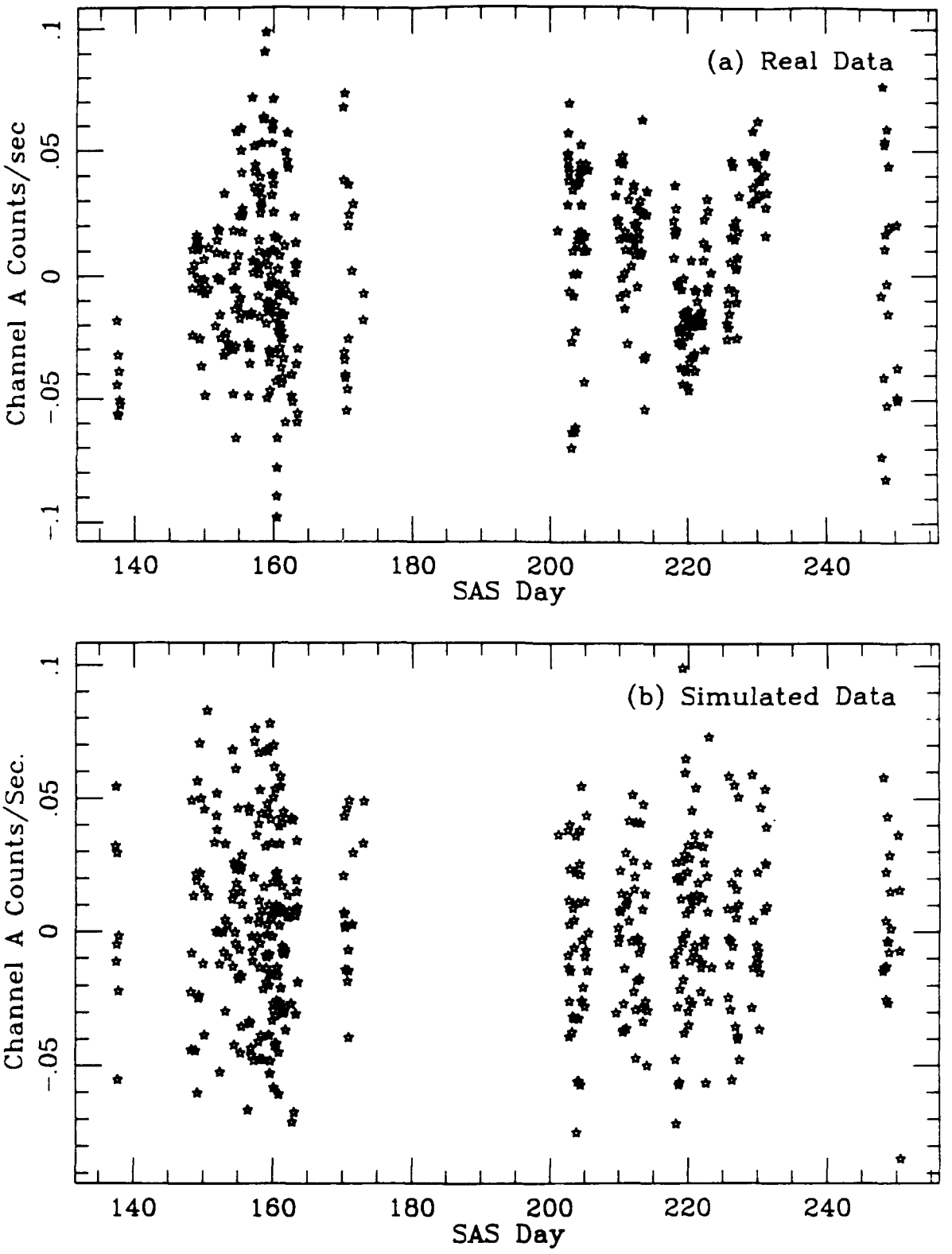

Figure 4.2.6: (a) Section of real channel A data.
(b) Section of simulated channel A data.

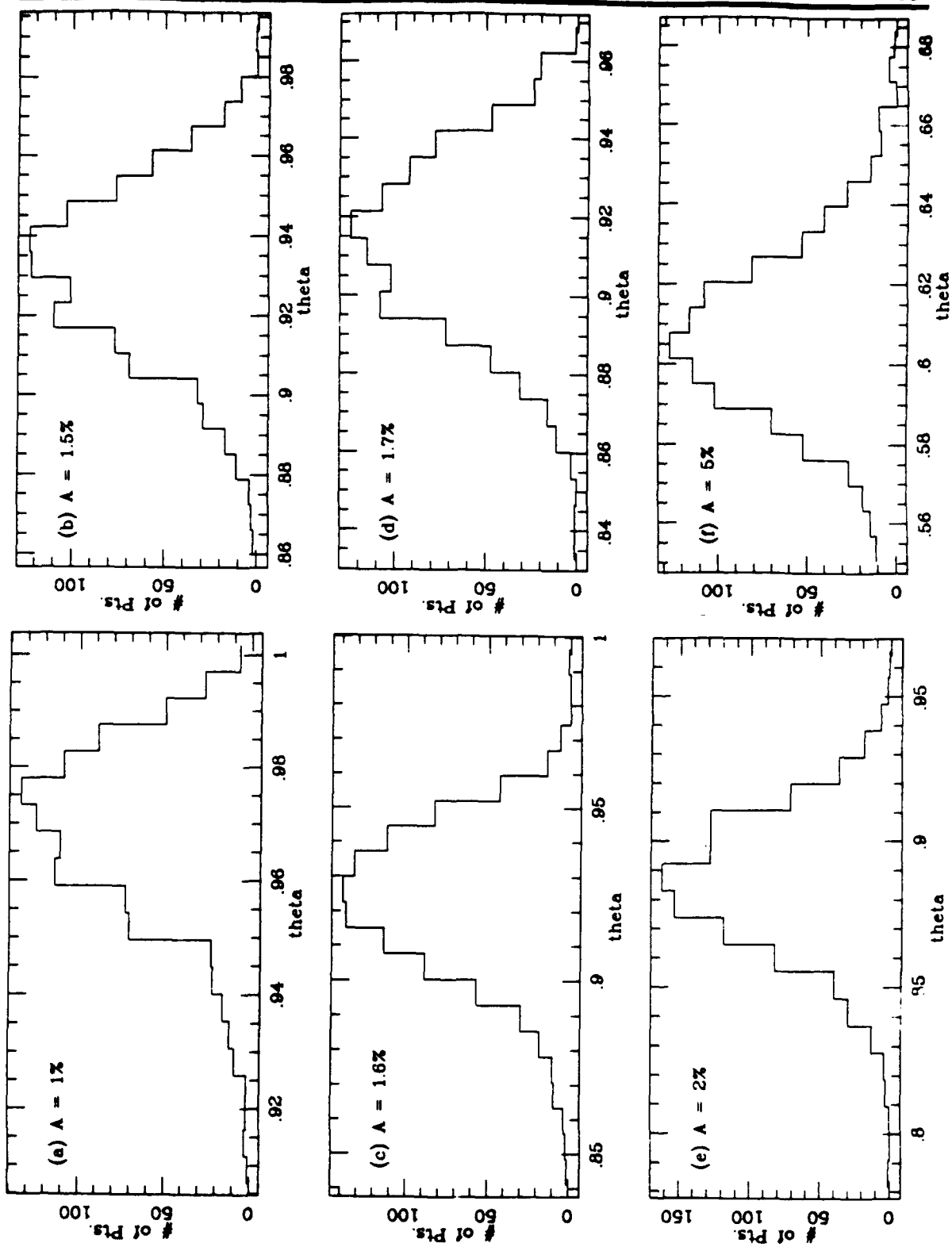

Figure 4.2.7: Histograms from the Monte Carlo simulation for various amplitudes of oscillation, A, at $\prod = 7.75^{h}$.

thousand which would yield that value or higher. This corresponds to 99.7% or roughly 3σ. In table 3, as explained in chapter 4.1, P is the probability that the observed period is due to random fluctuations and upper limit is the percentage periodic amplitude upper limit generated by the Monte Carlo simulation. In the table 3a we choose Θ corresponding to the biggest maximum near the period due to the uncertainty of the exact value (MB quote several periods). We exclude the improved MB section of the data from table 3a and will treat it separately in chapter 4.2.3

TABLE 3a
Results for $\prod = 7.8^{d}$

Channel Data Section[1]	Θ^{2}	P^{3}	3σ Upper Limit
A: Decay Phase	.95	.54	2.15%
A: Ramp	.955	.67	7.3%
B: Decay Phase	.985	.85	4.1%
H: Decay Phase	.987	.87	5.3%

TABLE 3b
Results for $\prod = 7.75^{h}$

Channel Data Section[1]	Θ^{4}	P^{3}	Upper Limit
A: Decay Phase	.995	.95	1.1%
A: Improved MB	.998	.98	6.0%
A: Ramp	.998	.98	4.17%
B: Decay Phase	1.0	1.0	3.85%
H: Decay Phase	1.0	1.0	3.17%

1. A, B, and H refer to Center Slat A, Center Slat B and B/A respectively.
2. From figure 4.2.7 where we choose the biggest max nearby.
3. Two sided F test from chapter 4.1 via computer (Press, 1988)
4. From figure 4.2.7.

4.2.3 MB's Data

MB based their periodicity claims on the section of data from SAS day 285 to 322. Figure 4.2.8a depicts the Stellingwerf procedure carried out on this range. There is a minimum theta of .70 at 7.84^d and the probability that this value of theta is due to random fluctuations, P, is negligible. The percent amplitude, from figure 4.2.1e is ~ 40%. The region from day 308 to 322 is largely noise. This section of data is basically the section which we called the ramp and, as we showed in section 4.2.2, it exhibits minimal periodicity. We take this section of data off of the MB data to get the improved MB data. Figures 4.2.8b and c show the periodicity searches carried out in these regions. We find a broad minimum about 8.27^d with a theta value of .575 and negligible P. This is the *only* section of data for which there is *any* strong periodic behavior. The improved MB section represents ~22 days or about three cycles. We will discuss the implications of these facts in chapter 4.3

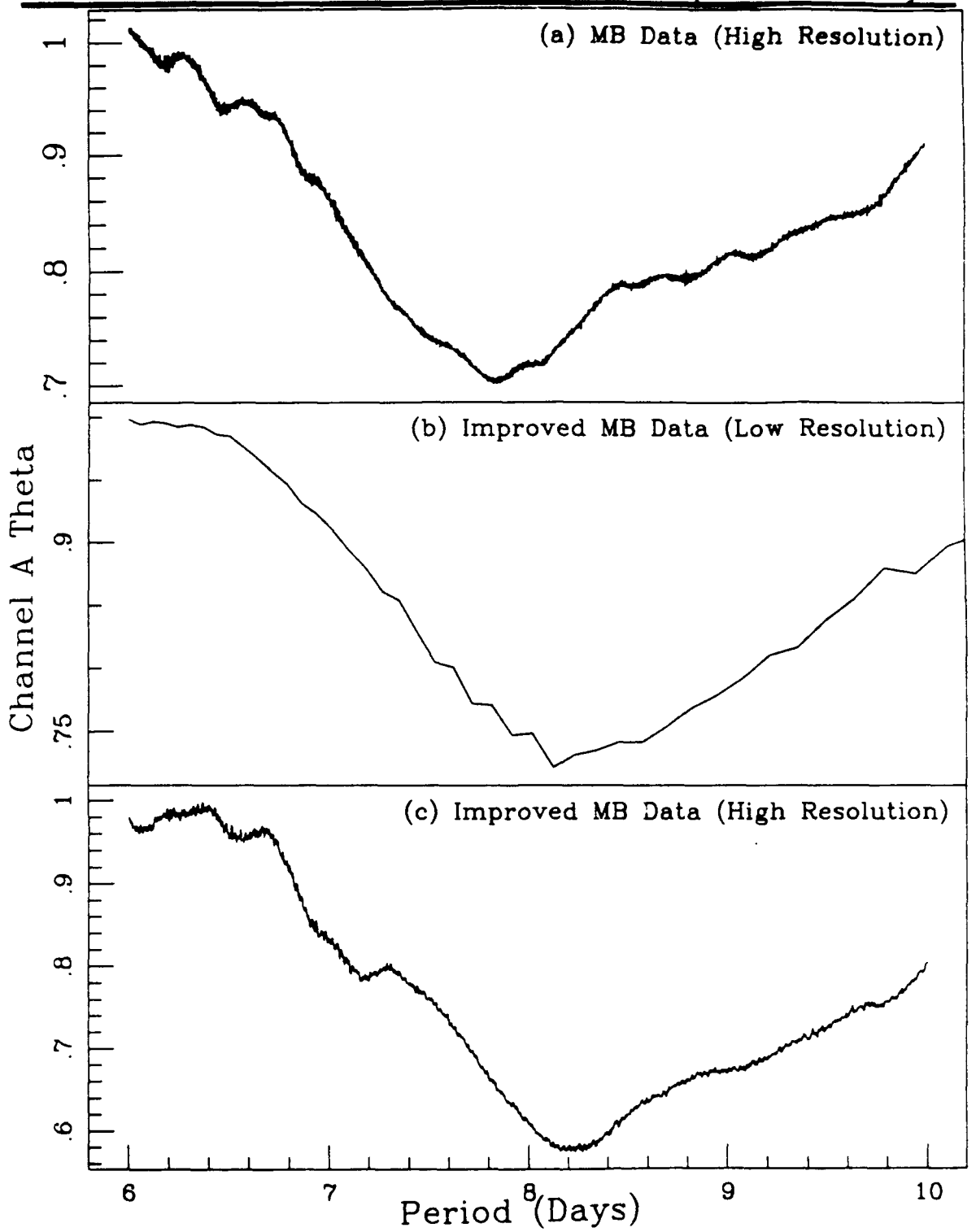

Figure 4.2.8: (a) Stellingwerf procedure on channel A MB phase at $\prod = 7.8^{d}$.
(b) Low res. Stellingwerf procedure on channel A improved MB phase
(c) High res.Stellingwerf procedure on channel A improved MB phase.

4.3 Conclusions

In chapter 4.2 we derived upper limits on the periodicity of the X-ray spectrum of A0620. For the 7.75^h period we found that the 3σ upper limit on the amplitude is 4.17% in the A channel ramp. We showed that apart from one twenty day period, the 3σ upper limit on the amplitude for the 7.8^d period is 7.3%.

It is perhaps not surprising that we see no evidence for the 7.75^h optical orbital period. This period was determined by MR through photometric and spectroscopic observations. There are no eclipse phenomena. One credible mechanism which might impress this period onto the X-ray spectrum is electron scattering from a high density electron cloud. If matter is accreting via Roche lobe overflow, we expect such a cloud near the L1 point where the streaming matter impacts into the accretion disk (figure 4.3).

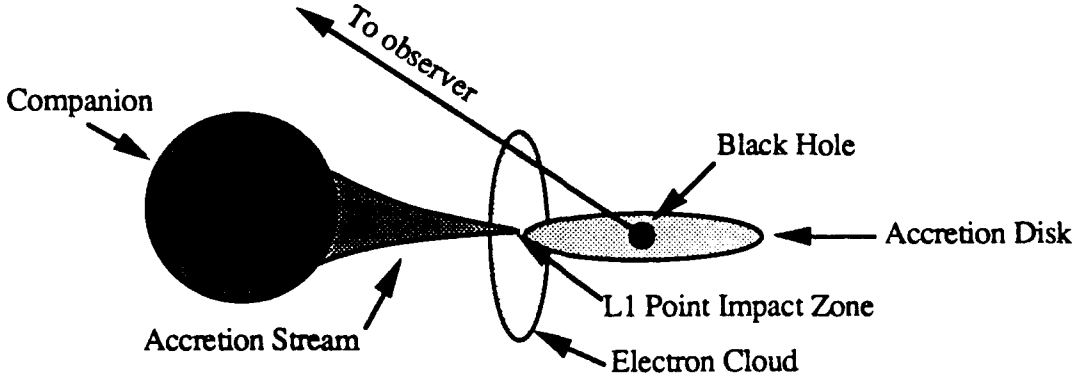

Figure 4.3: Diagram of electron cloud from the impact of the accretion stream into the accretion disk softening photons in observer's line of sight.

These electrons would scatter the X-rays and soften the resultant spectrum. Checking the B/A hardness ratio would reveal this softening to us. We expect to see this scattering during the decay phase of the nova when mass flow rates

are high. If we saw such periodicity it would imply that the system was accreting via Roche lobe overflow and that we were at a fairly high inclination angle with respect to the binary plane (chapter 1, figure 1.1) The fact that we see no evidence for this periodicity suggests that either the system is accreting via Roche lobe overflow, but is not at high inclination angle, or that the system is accreting via stellar wind capture at any reasonable inclination which satisfies the no eclipse condition. The severe hardness ratio amplitude 3σ upper limit of no more than 3.17% tends to rule out high inclination Roche lobe overflow models.

The light curves we obtained are extremely smooth. They are nearly perfect exponential decays (Figs. 4.2.1 and 4.2.2). Both of the non-steady state accretion theories presented in Chapter 1.3 predict such a decay. These theories are therefore in good agreement with our results.

We confirm the existence of three oscillations of a 7.8^d period between 7 January, 1976 and 13 February, 1976 previously reported by MB in the same data. This section of the data exhibits an amplitude of approximately 40% in the A channel. However, by virtue of our improved data reduction based on analysis of Crab observations detailed in chapters 2 and 3, we were able to show that in the rest of the data set, in excess of two hundred days, the A channel has a 3σ upper limit of 2.15% before this section and after it the 3σ upper limit in the A channel is 7.3%. The twenty two day section consists of three dips and three rises and could be represent 3 cycles of a 7.8^d period. It could also be three dips and three rises of interesting, but periodically insignificant, morphology in the X-ray light curve. We therefore find no evidence to substantiate the existence of a persistent 7.8^d period.

References

Avni, Y., Fabian, A. C., and Pringle, J. E. 1976, *M.N.R.A.S.*, **175**, 297.

Bevington, P. R. 1969, *Data Reduction and Error Analysis for the Physical Sciences*, New York; McGraw Hill Inc.

Boley, F. and Wolfson, R. 1975, *IAU Circ.*, No 2819.

Bregman, J., Butler, D., Kemper, E., Koski, A., Kraft, R. P., and Stone, R. P. S. 1973, *Ap. J. (Letters)*, **185**, L117.

Cannizzo, J. K., Lee, H. M., and Goodman, J. 1990, *Ap. J.*, **351**, 38.

Cannizzo, J. K., Ghosh, and Wheeler, J. C. 1982, *Ap. J. (Letters)*, **260**, 1982.

Carpenter, G. F., Eyles, C. J., Skinner, G. K., Willmore, A. P., and Wilson, A. M. 1976, *M.N.R.A.S.*, **176**, 397.

Chevalier, C., Janot-Pacheco, E., Mauder, H., and Ilovaisky, S. A. 1980, *A&A*, **81**, 348

Citterio, O., Conti, G., Di Benedetto, P., Tanzi, E. G., Perola, G. C., White, N. E., Charles, P. A., and Sandford, P. W. 1976, *M.N.R.A.S. (Letters)*, **175**, 35.

Coe, M. J., Engel, A. R., and Quenby, J. J. 1976, *Nature (Letters)*, **259**, 544.

Cowley, A. P., Crampton, D., Hutchings, J. B., Remillard, R., and Penfold, J. E. 1983, *Ap. J.*, **272**, 118.

Craft, H. D. Jr. 1975, *IAU Circ.*, No.2822.

Doxsey R., Jernigan, G., Hearn, D., Bradt, H,. Buff, J., Clark, G., W., Delvaille, J., Epstein, A., Joss, P. C., Matilsky, T., Mayer, W., McClintock, J., Rappaport, S., Richardson, J., and Schnopper, H. 1976, *Ap. J. (Letters)*, **203**, L9.

Eachus, L., Wright, E., and Liller, W. 1976, *Ap. J. (Letters)*, **203**, L17.

Eardley, D. M., and Lightman, A. P. 1975, *Ap. J.*, **200**, 187.

Elvis, M., Page, C. G., Pounds, K. A., Ricketts, M. J., and Turner, M., J., L. 1975, *Nature (Letters)*, **257**, 656.

Griffiths, R. E., Ricketts, M. J. and Cooke, B. A., *M.N.R.A.S.*, **177**, 429.

Hameury, J. M., King, A. R., and Lasota, J. P. 1986, *A&A*,**162**, 71.

Hameury, J. M., King, A. R., and Lasota, J. P. 1990, *Ap. J.*, **353**, 585.

Haswell, C. A., and Shafter, A. W. 1990, *Ap. J. (Letters)*, **359**, L47.

Hayakawa, S. 1976, *Ap. J. (Letters) Preprint.*

Huang, M. and Wheeler, J. C. 1989, *Ap. J.*, **343**, 229.

Hwang, U. 1988 *MIT Bachelor of Science Thesis.*

Ichimaru, S. 1977, *Ap. J.*, **214**, 840.

Johnston, H. M., Kulkarni, S. R., and Oke, J. B. 1989, *Ap. J.*, **345**, 492.

Kaluzienski, L. J., Holt, S. S., Boldt, E. A., and Serlemitsos, P. J. 1977, *Ap. J.*, **212**, 203.

Kestenbaum, H. L., Cohen, G. G., Long, K. S., Novick, R., Silver, E. H., Weisskopf, M., C., and Wolff, R. S. 1976, *Ap. J.*, **208**, 27.

Kleinmann, S. G., Brecher, K., and Ingham, W. H. 1976, *Ap. J.*, **207**, 532.

de Kool M. 1988, *Ap. J.* **334**, 336.

de Kool M. 1988, *Ap. J. Preprint.*

Lightman, A. P. 1974a, *Ap. J.*, **194**, 419.

Lightman, A. P. 1974b, *Ap. J.*, **194**, 429.

Lightman, A. P., Eardly, D. M. 1974, *Ap. J. (Letters)*, **187**, L1.

Lin and Taam 1984, *High Energy Transients in Astrophysics*, S. E. Woosley, Ed., American Institute of Physics Conf. Proc. #115, 83.

Little, A. G., Crawford, D. F. and Murdoch, H. S. 1976, *Nature*, **261**, 113.

Lloyd, C., Noble, R., and Penston, M. V. 1977, *M.N.R.A.S.*, **179**, 675.

Long, K. S., and Kestenbaum, H. L. 1978, *Ap. J.*, **226**, 271.

Matilsky, T., Bradt, H. V., Buff, J., Clark, G. W., Jernigan, J. G. Joss, P. C., Laufer, B., and McClintock, J. 1976, *Ap. J. (Letters)*, **210**, L127.

Mazeh, T., van Paradijs, J., van den Heuvel, E. P. J. and Savonije, G. J. 1986,

A&A, **157**, 113.

McClintock, J. E., CFA Preprint Series No. 2333.

McClintock, J. E., Petro, L. D., Remillard, R. A., and Ricker, G., R. 1983, *Ap. J. (Letters)*, **266**, 27.

McClintock, J. E., Remillard, R. A., and Petro, L. D. 1983, *B.A.A.S.*, **15**, 1003.

McClintock, J. E., and Remillard, R. A.,1986, *Ap. J.*, **308**, 110.

Mineshige, S., and Wheeler, J. C. 1989, *Ap. J.*, **343**, 241.

Mineshige, S., Tuchman, Y., and Wheeler, J. C. 1990, *Ap. J.*, **359**, 176.

Murdin, P., Allen, D. A., Morton, D. C.1980, *M.N.R.A.S.*, **192**, 709.

Oke, J. B. 1977, *Ap. J.*, **217**, 181.

Oke, J. B., and Greenstein, J. L., 1977, *Ap. J.*, **211**, 872.

Okuda, T., and Sakashita, S. 1977, *Astrophys. S. S.*, **47**, 385.

Owen, F., Balonek, T., Dickey, J., Terzian, Y. and Gottesman, S. 1976, *Ap. J. (Letters)*, **203**, L15.

Paczynski, B., 1974, *A&A*, **34**, 161.

Paczynski, B., 1983, *Ap. J. (Letters)*, **273**, L81.

Press, W. H., Flannery, B. P., Teukolsky, S. A. and Vetterling, W. T. 1988, *Numerical Recipies in C*, Cambridge; Cambridge University Press.

Pringle, J. E. 1976, *M.N.R.A.S.*, **177**, 65.

Ricketts, M. J., Pounds, K. A., and Turner, M. J. L. 1975, *Nature*, **257**, 658.

Remillard, R. A., 1990, Private Communication.

Remillard, R. A., 1991, Private Communication.

Scott, P. f. 1975, *IAU Circ.*, No. 2823.

Shakura, N. I., and Sunyaev, R. A. 1976, *M.N.R.A.S.*, **175**, 613.

Shakura, N. I., and Sunyaev, R. A. 1973, *A&A*, **24**, 337.

Shapiro, S. L. and Teukolsky, s. A. 1983, *Black Holes, Neutron Stars, and White Dwarfs*, New York; Wiley and Sons.

Stellingwerf, R. F., 1978, *Ap. J.*, **244**, 953.

Taylor, R. S. 1975, *MIT Orbiting X-Ray Observatory SAS-C.*

Tsunemi, H., Matsuoka, M., and Takagishi, K. 1977, *Ap. J.(Letters)*, **211**, L15.

van den Heuvel, E. P. J. 1983, *Accretion-Driven Steller X-Ray Sources*, eds. W. H. G. Lewin and E. P. J. van den Heuvel (Cambridge Cam. U. Press), 203.

Webbink, R. F. 1978, *A Provisional Optical Light Curve of the X-Ray Recurrent Nova V616 = A0620-00.*

Whelan, J. A. J., Ward, M. J., Allen, D. A., Danziger, I. J., Fosbury, R. A. E., Murdin, P. G., Penston, M. V., Peterson, B. A., Wampler, E. J., and Webster, B. L. 1977, *M.N.R.A.S.*, **180**, 657.

Woo, J. W., 1991, Private Communication.

Acknowledgements

I would like to thank the Hertz Foundation for having the faith in me to award me one of their fellowships. I would also like to thank the Air Force for allowing me the opportunity to perform my research.

Professor George W. Clark deserves much thanks. He has been a constant source of advice and encouragement and he has the remarkable talent of motivating me to do more than I thought I could do. His insights into the nature of physical processes and their research have resulted in more than one chapter in this thesis.

Special thanks to Dr. Ron Remillard who provided me with many suggestions about how best to analyze my data and acted as a sounding board for my ideas and results. He was very motivational and was a constant source of encouragement and inspiration.

I would especially like to thank Jonathan Woo who tolerated many a stupid question and provided many helpful suggestions. He had the patience to explain his ideas to me in a clear manner and I am sure that he will have a long and successful career as an educator.

I thank Dr. Ed Morgan for his invaluable knowledge of the SAS system and for providing numerous computer programs. I am indebted to Richard Brezina who either wrote, or translated, the majority of the computer code in the reduction package. I would also like to thank the following individuals, who are listed in no particular order: Gene Magnier, Bob Rutledge, Prof. Walter Lewin, Andy Silber, Bruce Grossan, Una Huang, Kenton Phillips and Pat Mock. Finally, I would like to thank my roommate, my friends, and the MIT Rugby Football Club for conspiring to keep me sane for the past two years.